Aircraft-based observation of meteoric material in lower stratospheric aerosol particles between 15 and 68°N

Johannes Schneider[1], Ralf Weigel[2], Thomas Klimach[1], Antonis Dragoneas[1], Oliver Appel[1], Andreas Hünig[1], Sergej Molleker[1], Franziska Köllner[1], Hans-Christian Clemen[1], Oliver Eppers[3], Peter Hoppe[1], Peter Michael Hoor[4], Christoph Mahnke[5], Martina Krämer[6], Christian Rolf[7], Jens-Uwe Grooß[7], Andreas Zahn[8], Florian Obersteiner[9], Fabrizio Ravegnani[10], Alexei Oulanovsky[11], Hans Schlager[12], Monika Scheibe[13], Glenn S. Diskin[14], Joshua Paul DiGangi[14], John B. Nowak[14], Martin Zöger[15], and Stephan Borrmann[16]

[1]Max Planck Institute for Chemistry
[2]Institute for Physics of the Atmosphere
[3]Johannes Gutenberg University of Mainz
[4]University Mainz
[5]Johannes Gutenberg-Universität
[6]FZ Jülich, Germany
[7]Forschungszentrum Jülich
[8]Karlsruhe Institute of Technology (KIT)
[9]Karlsruhe Institute for Technology
[10]CNR
[11]CAO
[12]DLR
[13]Unknown
[14]NASA Langley Research Center
[15]DLR Oberpfaffenhofen
[16]Max Planck Institute for Chemistry, Mainz , Germany

November 23, 2022

Abstract

Particles containing meteoric material were observed in the lower stratosphere during five aircraft research missions in recent years. Single particle laser ablation technique in a bipolar configuration was used to measure the chemical composition of particles in a size range of approximately 150 nm to 3 µm. The five aircraft missions, conducted between 2014 and 2018, cover a latitude range from 15 to 68°N. In total, more than 330 000 single particles were analyzed. A prominent fraction (more than 50 000) of the analyzed particles was characterized by strong abundances of magnesium, iron, and rare iron oxide compounds, together with sulfuric acid. This particle type was found almost exclusively in the stratosphere and is interpreted as meteoric material immersed or dissolved in stratospheric sulfuric acid particles. Below the tropopause the fraction of this particle type decreases sharply. However, small abundances were observed below 3000 m a.s.l. in the Canadian Arctic and also at the Jungfraujoch high altitude station (3600 m a.s.l.). Thus, the removal pathway by sedimentation and/or mixing into the troposphere is confirmed. Our data show that particles containing meteoric material are present in the lower stratosphere in very similar relative abundances, regardless of latitude or season. This finding suggests that the meteoric material is transported from the mesosphere into the stratosphere in the downward branch of the Brewer-Dobson-Circulation and efficiently distributed

towards low latitudes by isentropic mixing. As a result, meteoric material is found in particles of the stratospheric Junge layer at all latitudes.

Aircraft-based observation of meteoric material in lower stratospheric aerosol particles between 15 and 68°N

Johannes Schneider[1], Ralf Weigel[2], Thomas Klimach[1], Antonis Dragoneas[1,2], Oliver Appel[1,2], Andreas Hünig[1,2], Sergej Molleker[1,2], Franziska Köllner[1], Hans-Christian Clemen[1], Oliver Eppers[1,2], Peter Hoppe[1], Peter Hoor[2], Christoph Mahnke[2,1], Martina Krämer[3], Christian Rolf[3], Jens-Uwe Grooß[3], Andreas Zahn[4], Florian Obersteiner[4], Fabrizio Ravegnani[5], Alexey Ulanovsky[6], Hans Schlager[7], Monika Scheibe[7], Glenn S. Diskin[8], Joshua P. DiGangi[8], John B. Nowak[8], Martin Zöger[9], Stephan Borrmann[2,1]

[1]Particle Chemistry Department, Max Planck Institute for Chemistry, Mainz, Germany
[2]Institute for Physics of the Atmosphere, Johannes Gutenberg University, Mainz, Germany
[3]Forschungszentrum Jülich, Institute of Energy and Climate Research (IEK-7), Jülich, Germany
[4]Karlsruhe Institute of Technology (KIT), Institute for Meteorology and Climate Research, Karlsruhe, Germany
[5]Institute of Atmospheric Sciences and Climate, ISAC-CNR, Bologna, Italy
[6]Central Aerological Observatory, Pervomayskaya 3, Dolgoprudny, Russia
[7]Institute of Atmospheric Physics, German Aerospace Center (DLR) Oberpfaffenhofen, Wessling, Germany
[8]NASA Langley Research Center, MS 483, Hampton, VA, USA
[9]Flight Experiments Department, German Aerospace Center (DLR) Oberpfaffenhofen, Wessling, Germany

Correspondence to: Johannes Schneider (johannes.schneider@mpic.de)

Key points:

- Meteoric material in lower stratospheric particles detected at all latitudes between 15 and 68°N
- These particles contain mainly sulfuric acid and thus are sediments from the stratospheric Junge layer
- Downward transport from the mesosphere via Brewer-Dobson-Circulation and isentropic mixing efficiently distributes meteoric material meridionally.

Abstract

Particles containing meteoric material were observed in the lower stratosphere during five aircraft research missions in recent years. Single particle laser ablation technique in a bipolar configuration was used to measure the chemical composition of particles in a size range of approximately 150 nm to 3 µm. The five aircraft missions, conducted between 2014 and 2018, cover a latitude range from 15 to 68°N. In total, more than 330 000 single particles were analyzed. A prominent fraction (more than 50 000) of the analyzed particles was characterized by strong abundances of magnesium, iron, and rare iron oxide compounds, together with sulfuric acid. This particle type was found almost exclusively in the stratosphere and is interpreted as meteoric material immersed or dissolved in stratospheric sulfuric acid particles. Below the tropopause the fraction of this particle type decreases sharply. However, small abundances were observed below 3000 m a.s.l. in the Canadian Arctic and also at the Jungfraujoch high altitude station (3600 m a.s.l.). Thus, the removal pathway by sedimentation and/or mixing into the troposphere is confirmed. Our data show that particles containing meteoric material are present in the lower stratosphere in very similar relative abundances, regardless of latitude or season. This finding suggests that the meteoric material is transported from the mesosphere into the stratosphere in the downward branch of the Brewer-Dobson-Circulation and efficiently distributed towards low latitudes by isentropic mixing. As a result, meteoric material is found in particles of the stratospheric Junge layer at all latitudes.

1 Introduction

Aerosol particles in the upper troposphere/lower stratosphere (UTLS) play an important role in the Earth's radiative budget: Firstly, by direct scattering of sunlight back to space, secondly and likely more importantly, by influencing homogeneous and heterogeneous cirrus cloud formation in the upper troposphere (UT). The total indirect forcing due to ice formation in the atmosphere was recently estimated to be around + 0.27 W m^{-2} [*Gettelman et al.*, 2012]. Furthermore, aerosol particles in the UTLS provide surfaces for heterogeneous chemical reactions. Generally, the dominating sources of aerosol particles and their precursor gases, like organic and sulfur-containing compounds for secondary aerosol formation or primary particles like dust, sea spray, black carbon, or biomass burning particles, are on the Earth's surface. These sources can be both natural and anthropogenic. In contrast, an exclusively natural source of a certain fraction of atmospheric particles is located outside the Earth's atmosphere, causing an ambling but continuous particle import of cosmic origin. The magnitude of cosmic material entering the Earth's atmosphere is currently estimated to range at 43 ± 14 t d^{-1} (tons per day) [*Plane*, 2012; *Carrillo-Sánchez et al.*, 2016]. Besides oxygen, major elements of meteoric material are Fe, Mg, and Si, which are found with roughly equal proportions in chondritic meteorites; the most abundant minor elements are C, S, Al, Na, Ca, and Ni [*Lodders and Fegley Jr.*, 1998; *Hoppe*, 2009; *Plane et al.*, 2015]. First detection of magnesium emission lines in the night sky spectrum and the conclusion that at least part of atmospheric magnesium is of meteoric origin were reported by *Hicks et al.* [1972].

About 8 t d^{-1} of the cosmic dust particles (with diameters between ~ 1 µm and ~300 µm) are completely ablated during entry in the Earth's atmosphere at altitudes around 90 km [*Plane*, 2003; *Carrillo-Sánchez et al.*, 2016]. Quenching of evaporated compounds is expected to cause their rapid re-nucleation in the mesosphere to form new particles of the size of a few nanometers which are commonly referred to as meteoric smoke particles (MSP) [*Saunders et al.*, 2012; *Plane et al.*, 2015; *Hervig et al.*, 2017]. In MSP, the relatively volatile elements Na and K are enhanced compared to the main components Fe, Mg and Si [*Vondrak et al.*, 2008], because the more volatile elements are more readily released from the meteoric body by ablation than the more refractory species Ca, Al and Ti [*Carrillo-Sánchez et al.*, 2016; *Plane et al.*, 2018]. Recent remote-sensing and in-situ measurements in the mesosphere indicated that Fe and Mg are the main constituents of MSP [*Hervig et al.*, 2012; *Rapp et al.*, 2012]. MSP have been identified to act as ice nuclei for noctilucent clouds in the mesopause region [e.g., *Alpers et al.*, 2001; *Gumbel and Megner*, 2009; *Megner and Gumbel*, 2009; *Rapp et al.*, 2010] and therefore they are assumed to impact polar mesospheric summer echoes [*Rapp and Lübken*, 2004; *Megner et al.*, 2006]. As MSP are too small to sediment gravitationally, it is widely assumed that MSP are drained from the mesosphere into the stratosphere most efficiently due to the air mass subsidence within the polar winter vortex, in a timescale of months [*Plumb et al.*, 2002; *Curtius et al.*, 2005; *Megner et al.*, 2008; *Plane*, 2012; *Saunders et al.*, 2012; *Weigel et al.*, 2014; *Plane et al.*, 2015; *Kremser et al.*, 2016]. In the stratospheric aerosol layer [*Junge et al.*, 1961; *Junge and Manson*, 1961; *Kremser et al.*, 2016], consisting mainly (to about 70 wt%) of sulfuric acid solution (H_2SO_4-H_2O) droplets [*Lazrus et al.*, 1971; *Rosen*, 1971; *Lazrus and Gandrud*, 1974; 1977; *Sedlacek et al.*, 1983; *Gandrud et al.*, 1989; *Arnold et al.*, 1998], it is expected that the MSP dissolve in the droplets [*Murphy et al.*, 1998; *Cziczo et al.*, 2001; *Saunders et al.*, 2012; *Murphy et al.*, 2014]. These Junge layer droplets are typically in the size range of 100-200 nm [*Plane et al.*, 2015; *Kremser et al.*, 2016], such that a dilute solution of highly soluble ferrous/ferric sulfate and hydrated magnesium sulfate and silicic acid is formed [*Saunders et al.*, 2012].

As has recently been shown by *Subasinghe et al.* [2016], about 95 % of cosmic bodies of sizes greater than 1 mm in diameter undergo fragmentation upon entering the Earth's atmosphere, thereby forming unablated meteoric fragments (MF) of presumably submicron size. If such fragments were formed, these particle may sediment directly into the lower stratosphere. It has been suggested that MF may play a role in polar stratospheric cloud (PSC) formation, thereby influencing polar ozone destruction [*Voigt et al.*, 2005; *James et al.*, 2018]. In simulations focused on the characteristics of PSC in the model CLaMS (Chemical Lagrangian Model of the Stratosphere), the PSC observations could

only be reproduced when including heterogeneous nucleation of NAT [*Grooß et al.*, 2014] and ice particles [*Tritscher et al.*, 2019] on foreign nuclei which likely would be meteoric dust.

Additionally, certain amounts of cosmic particulate material enter the Earth's atmosphere as Interplanetary Dust Particles (IDP) which, if smaller than 1 µm in diameter, are too small to experience any ablative altering during atmospheric entry at all. The origin of IDP is mainly attributed to collisions of asteroids, sublimation of comets and long-decayed cometary trails [*Plane*, 2003; 2012]. In terms of the size-segregated mass influx of cosmic particles [*Plane*, 2003; 2012], the contribution of submicrometer sized IDP to the atmospheric aerosol load is estimated to range at about 150 t per year. Thus, the contribution of IDP to the overall input of cosmic aerosol material with regard to mass is small. However, the import of IDP is likely a continuous process compared to sporadic events of meteoric entries that produce by far more MSP per event. Therefore, an ambling and persistent import of cosmic aerosol (by number) should be considered in relationship to the infrequent but then excessively effective ablation/fragmentation events releasing huge amounts of MSP and MF in the atmosphere.

The existence of particles containing meteoric material in the lower stratosphere has been shown by direct in-situ observations: *Mossop* [1965] reported on insoluble inclusions found in stratospheric particles sampled at 20 km by the U-2 aircraft and suggested a meteoric origin of these particles. Later, aircraft-based in-situ aerosol mass spectrometry allowed for more detailed composition measurements. Mass spectrometric measurements in the tropical and mid-latitude lower stratosphere at altitudes up to 19 km showed a significant fraction of particles containing meteoric material and sulfuric acid [*Murphy et al.*, 1998; *Cziczo et al.*, 2001; *Froyd et al.*, 2009; *Murphy et al.*, 2014]. Indirect evidence for the existence of meteoric aerosol material in the Arctic lower stratosphere up to 20 km altitude was reported by *Curtius et al.* [2005] and *Weigel et al.* [2014], who observed, with increasing altitude inside the Arctic winter vortex, an increasing fraction (up to 70%) of non-volatile particles (thermally stable on exposure to 250°C, with diameters of 10 nm to a few micrometers). From impactor samples of submicrometer particles within the Artic stratosphere during the winters of the years 2010 and 2011 the chemical composition and the morphology of various refractory (electron beam stable) particles was analyzed. Fe-rich particles, Ca-rich particles, silicates, silicate /carbon mixed particles and mixed metal particles from different sources, such as meteoric material, space debris and to lower extent terrestrial sources [*Ebert et al.*, 2016].

Here we report on aircraft-based observations in the lower stratosphere at different altitudes, latitudes and seasons: Western Europe, spring (April 2014) and summer (July 2018); Mediterranean, summer (August-September 2016); tropics/subtropics, summer (July-August 2017 and August 2018); North America/Northern Atlantic, winter (January-February 2018). In all data sets we observed a distinct particle type in the lower stratosphere that can be interpreted as particles containing meteoric material, dissolved in or coated by sulfuric acid. We discuss mass spectral composition, size distribution, vertical profiles, latitudinal distribution, and cross-tropopause transport of the meteoric particles.

2 Measurements and Methods

2.1 Aircraft missions

This study includes stratospheric and upper tropospheric data obtained during five aircraft-based research campaigns, plus two data sets from low altitudes (below 3600 m a.s.l). The individual projects are described briefly in the following. The flight tracks of all upper tropospheric and stratospheric research flights included here are depicted in Figure 1. General information and data on the aircraft projects are given in Table 1.

2.1.1 ML-CIRRUS

The field campaign ML-CIRRUS (Mid-Latitude Cirrus) was conducted in March and April 2014 out of Oberpfaffenhofen, Germany, using the research aircraft HALO (High Altitude and Long Range Research Aircraft). A total of 16 flights (including test flights) were carried out, aiming mainly

for the analysis of cirrus clouds by in-situ and remote sensing methods. Most of the flight time (in total 88 hours) was spent in the upper troposphere and lower stratosphere. Aerosol mass spectrometer data were recorded during 15 flights which are included in this study. A detailed overview on the mission is given by *Voigt et al.* [2017].

2.1.2 StratoClim

Two aircraft based research campaigns were conducted in the project StratoClim (Stratospheric and upper tropospheric processes for better climate predictions) which is a collaborative research project funded by the European Commission. The first phase of StratoClim took place at Kalamata airport, Greece, in August and September 2016. The aim of the mission was to study atmospheric composition in the Eastern Mediterranean region, including the remote influence of the Asian monsoon anticyclone (AMA) outflow. Three research flights were conducted. The second phase of StratoClim took place at the Tribhuvan International Airport of Kathmandu, Nepal, in July and August 2017 [*Höpfner et al.*, 2019]. Eight scientific flights were carried out over Nepal, India and Bangladesh. The flight paths spanned latitudes from 21° N to 27° N and longitudes from 79° E to 90° E (see Figure 1). This field campaign constituted the main phase of the StratoClim aircraft operations and aimed at the direct study of the AMA.

2.1.3 ND-MAX/ECLIF-2

The ND-MAX/ECLIF-2 (NASA/DLR-Multidisciplinary Airborne eXperiments/Emission and CLimate Impact of alternative Fuel) mission focused on aircraft emissions with a dedicated aircraft chasing field experiment over South-West Germany. For this mission, the implementation of the research instrumentation on the NASA DC-8 aircraft took place at Palmdale, CA, USA. The ferry flights from Palmdale to Germany on January 13, 2018 and back on February 3 and 4, 2018, were used as measurement flights. These flights reached latitudes up to 68°N (see Fig. 1), longitudes as far as 120° W, and penetrated deep into the winter stratosphere at around 11 km altitude.

2.1.4 CAFE-Africa

CAFE-Africa (Chemistry of the Atmosphere Field Experiment in Africa) was conducted with HALO in August 2018 out of Sal on the Cape Verde Islands. The main objective was to study the African monsoon outflow in the upper troposphere over the Atlantic Ocean. This study includes only data which were obtained during three research flights reaching the stratosphere. These flights took place on August 15, August 24, and September 07, 2018, the latter being the ferry flight back to Germany. The flight tracks of these three flights are included in Figure 1.

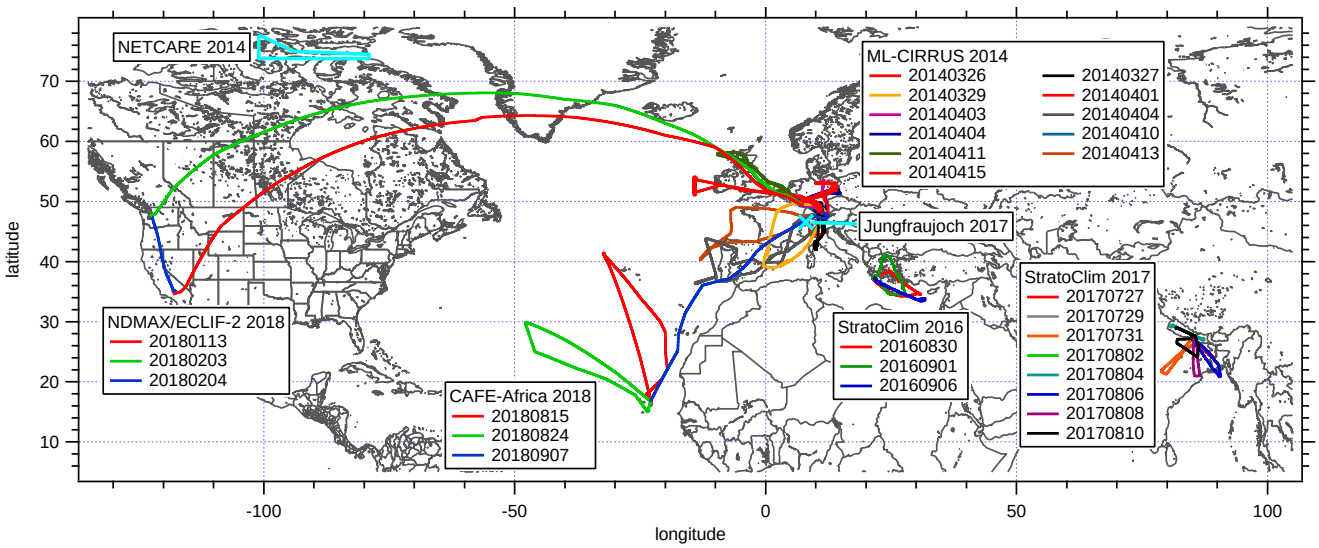

Figure 1: Map of the flight tracks of all UTLS research flights used in this study. Additionally the locations of the low altitude measurements are indicated: Jungfraujoch (3600 m a.s.l.) and operation range of the NETCARE flights (0 – 3000 m a.s.l.).

Table 1. Overview on the UTLS data sets used in this study.

Project	ML-CIRRUS	StratoClim 2016	StratoClim 2017	ND-MAX	CAFE-Africa
Time	Mar – Apr 2014	Aug – Sep 2016	Jul – Aug 2017	Jan - Feb 2018	Aug – Sep 2018
Measurement region	Western Europe	Eastern Mediterranean	South Asia	U.S. to Europe	Atlantic Ocean
Aircraft	HALO (G550)	M-55 Geophysica	M-55 Geophysica	NASA DC-8	HALO (G550)
Instrument	ALABAMA	ERICA	ERICA	ERICA	ALABAMA
No. of flights used in this study	15	3	8	3	3
Altitude range (km)	up to 13.8 km	up to 20.2 km	up to 20.5 km	up to 11 km	up to 14.5 km
Theta range (K)	276 - 387	295 - 490	310 - 480	276 – 340	295 - 380
Latitude range (° N)	36.3 – 57.5	33.4 – 41.0	20.8 - 29.5	34.6 – 68.1	15.0 – 48.2
PV range (PVU)	0 - 10	0 – 24	0 - 22	0 - 8	0 - 10
Number of single particle mass spectra	24833	11709	138119	98598	65104
Number of detected meteoric particles	3140	2412	18688	23138	3310

2.2 Aircraft based measurements and data analysis

2.2.1 Aerosol mass spectrometer operated during ML-CIRRUS and CAFE-Africa

The aircraft-based laser ablation aerosol mass spectrometer (ALABAMA) has been described in detail in *Brands et al.* [2011] and *Köllner et al.* [2017]. Briefly, the ALABAMA is a bipolar single particle analysis instrument that samples aerosol particles from ambient air through a constant pressure inlet and an aerodynamic lens. The sampled particle size range (vacuum aerodynamic diameter, d_{va}) was between about 200 and 1000 nm during ML-CIRRUS and between 200 nm and 3000 nm during CAFE-Africa. Having passed the aerodynamic lens, the particles are accelerated into the vacuum chamber. The particles are detected by two 405 nm laser diodes and their velocity information is used to determine their vacuum aerodynamic diameter (d_{va}, *DeCarlo et al.* [2004]) and to trigger a laser shot of the ablation laser (quadrupled Nd:YAG, 266 nm) that hits the particles in the ionization region of the bipolar time-of-flight mass spectrometer. Aerosol particles were sampled through the HALO aerosol submicrometer inlet [HASI, *Andreae et al.*, 2018]. The inlet was mounted on the upper side of the fuselage of the aircraft. Inside the aircraft, the sampled aerosol particles were guided through a 2.9 m long stainless steel sampling line with an inner diameter of 5 mm to the ALABAMA. The calculated transmission efficiency of this sampling line is shown in the supplement (Fig. S10). During ML-CIRRUS, the ALABAMA was operative during 15 flights and analyzed more than 24000 ambient aerosol particles (see Table 1). From CAFE-Africa, we include here a subset of three flights where HALO reached the stratosphere. In these three flights ALABAMA sampled and analyzed more than

65000 particles. The higher efficiency and higher upper size cut-off (see above) of ALABAMA in CAFE-Africa compared to ML-CIRRUS are due to several instrumental improvements like a new aerodynamic lens system and delayed ion extraction. In both HALO missions, an optical particle spectrometer (Grimm 1.129 "Sky-OPC") was installed in the same rack as ALABAMA and measured the total particle number concentration and size distribution for particles larger than 250 nm (manufacturer calibration) in diameter.

2.2.2 Aerosol mass spectrometer operated during StratoClim and ND-MAX

The mass spectrometer ERICA (ERC Instrument for Chemical composition of Aerosols) is a new development, combining single particle laser ablation and flash vaporization/ionization technique. It was designed for fully automated operation on the high altitude research aircraft M-55 "Geophysica" during the StratoClim project and was later re-configured to be operated on the NASA DC-8 during the ND-MAX/ECLIF-2 mission. Here we use only data obtained using the laser ablation part of ERICA (ERICA-LAMS). The principle design is similar to that of ALABAMA: The aerosol particles are sampled via a constant pressure inlet and an aerodynamic lens, detected in the vacuum chamber by two laser diodes (405 nm) and ablated by a pulsed quadrupled Nd:YAG laser (266 nm) operated without a wavelength separator in the laser head, thereby emitting also a small fraction of the energy in form of the first and second harmonic (1064 and 532 nm). The generated ions are analyzed in a bipolar time-of-flight mass spectrometer. The size range of ERICA-LAMS is approximately 100 – 5000 nm (d_{va}). During StratoClim, ERICA was operated on 11 research flights (three in 2016 and eight in 2017), and ERICA-LAMS analyzed about 150 000 single particles (see Table 1). During the three ferry flights conducted in the ND-MAX/ECLIF-2 project that are used here, ERICA-LAMS recorded more than 98 000 single particle mass spectra.

2.2.3 Single particle mass spectrometer data analysis

The aircraft data sets from all campaigns were analyzed using a consistent procedure to ensure comparability of the results. First, all data measured during one campaign were merged into one data set per campaign. This resulted in data sets containing individual spectra information of 11 709 particles (StratoClim 2016) to up to 138 119 particles (StratoClim 2017) as given in Table 1. These data sets were clustered using a fuzzy c-means algorithm (for a general description see *Bezdek et al.* [1984]; *Hinz et al.* [1999]; for an ALABAMA-specific description see *Roth et al.* [2016]), with a pre-selected number of 20 clusters. Only cations were considered for the clustering algorithm for two reasons: First, during ML-CIRRUS many anion mass spectra were too noisy. Second, the particle type of interest was found to be mainly characterized by the cation mass spectrum, containing magnesium and iron, as explained in the next section. Further clustering details are given in the supplement (Section 1.1 and Table S1). For quality assurance and uncertainty estimation, the clustering was repeated using different starting conditions and also different algorithms. The results showed only small deviations in the type of clusters and in the numbers of mass spectra attributed to the clusters (supplement, Section 1.2 and Table S2). Mean mass spectra (anions and cations) were calculated for each cluster and were used for the interpretation of the particle type associated with this cluster. Histograms of relative particle abundance were calculated for each cluster as function of altitude, potential temperature (Θ), and potential vorticity (PV).

The data sets from low altitudes (NETCARE, Jungfraujoch) were treated differently: Here we searched specifically for mass spectra using selected marker ions that were found in the high altitude data. This is explained later in detail (Section 3.7)

2.2.4 Auxiliary aircraft data

Water vapor (H_2O) was measured during ML-CIRRUS and StratoClim by the airborne Fast In-situ Stratospheric Hygrometer (FISH). This instrument uses Lyman-alpha photofragment fluorescence and is described in detail by *Zöger et al.* [1999]. The detection limit is reported to be below 0.4 ppmv, the uncertainty was determined to be about 8 – 30% for low H_2O mixing ratios (1 – 4 ppmv) and 6 – 8% between 4 and 1000 ppmv [*Meyer et al.*, 2015]. During ML-CIRRUS, FISH sampled the air through a forward facing inlet mounted on the upper fuselage of the HALO aircraft, whereas during StratoClim, the forward facing FISH inlet was mounted on the side of the fuselage of the Geophysica aircraft [*Afchine et al.*, 2018]. The forward facing inlet also samples cloud droplets and ice crystals which evaporate in the inlet, such that the FISH measurements refer to total water. We therefore restricted the data set to non-cloud conditions, by removing the data points where the H_2O saturation ratio was greater than 0.8. During ND-MAX/ECLIF-2, water vapor was measured using the Diode Laser Hygrometer (DLH) of NASA/LaRC [*Diskin et al.*, 2002]. During CAFE-Africa, water vapor was measured by SHARC (Sophisticated Hygrometer for Atmospheric ResearCh) based on direct absorption measurement by a tunable diode laser (TDL) system. The uncertainty of SHARC is 5% or ± 1 ppmv.

Ozone (O_3) was measured during ML-CIRRUS and CAFE-Africa by the Fast Airborne Ozone Monitor (FAIRO), whereas during StratoClim, O_3 was measured by the Fast Ozone Analyzer (FOZAN-II). Both FAIRO and FOZAN-II are based on dry chemiluminescence. Details can be found in *Yushkov et al.* [1999], *Ulanovsky et al.* [2001], and *Zahn et al.* [2012]. During ND-MAX, O_3 was measured by the UV photometric Ozone analyzer TE49 (Thermo Scientific).

Aerosol particle size distributions were measured during the StratoClim campaigns using a modified Ultrahigh Sensitive Aerosol Spectrometer (UHSAS-A), with a particle diameter range from 65 nm to 1000 nm. The modifications allowed for an airborne application range up to the extreme conditions in the stratosphere at a height of 20 km [*Mahnke*, 2018].

Basic meteorological parameters like pressure, temperature, as well as aircraft position and altitude were obtained during ML-CIRRUS and CAFE-Africa from the Basic HALO Measurement and Sensor System (BAHAMAS), during StratoClim from the Unit for Connection with the Scientific Equipment (UCSE), and during ND-MAX/ECLIF-2 from the NASA DC-8 facility instrumentation.

2.3 Meteorological reanalysis

For categorizing the observation locations, we use results of the model CLaMS (Chemical Lagrangian Model of the Stratosphere) interpolated onto the flight path [*McKenna et al.*, 2002a; *McKenna et al.*, 2002b; *Pommrich et al.*, 2014]. These model simulations were based on ERA-Interim re-analysis data [*Dee et al.*, 2011] from the European Centre of Medium Range Weather forecast (ECMWF). For meridional characterization we use equivalent latitude [*Lary et al.*, 1995] from these data sets. For vertical coordinate we use potential vorticity derived from ECMWF operational analysis data and potential temperature derived from observed pressure and temperature data.

2.4 Additional low altitude data sets

In order to investigate the possible occurrence of meteoric particles in the lower troposphere, we used two data sets from low altitudes: One data set was obtained during NETCARE (Network on Climate and Aerosols: Addressing Key Uncertainties in Remote Canadian Environments, *Abbatt et al.* [2019]), conducted in the Arctic out of Resolute Bay (Nunavut, Canada) in July 2014. The ALABAMA mass spectrometer was operated on board the Polar 6 aircraft (Alfred Wegener Institut – Helmholtz Zentrum für Polar- und Meeresforschung) and measured at altitudes between 0 and 3 km. Details of the campaign and the mass spectrometer data are given in *Köllner et al.* [2017]. During the INUIT-JFJ (Ice Nucleation Research Unit Jungfraujoch) campaign in January and February 2017, the ALABAMA was operated on the High Alpine Research Station Jungfraujoch. The mass spectrometer data are still

unpublished, but details on the campaign can be found in *Eriksen Hammer et al.* [2018] and *Gute et al.* [2019].

3 Results

3.1 Distinct particle type containing magnesium and iron ions

In all five upper tropospheric and lower stratospheric aircraft data sets, the clustering algorithm yielded a type of mass spectra with a mean cation mass spectrum characterized by high abundance of magnesium (Mg^+, m/z 24 for the major isotope, m/z 25 and 26 for the minor isotopes) and iron (Fe^+, m/z 56 for the major isotope, m/z 54 for the most abundant minor isotope). Also oxides of Fe (FeO^+, m/z 72; $FeOH^+$, m/z 73) were clearly detected. Further cations include sodium (Na^+, m/z 23), aluminum (Al^+, m/z 27), as well as minor signals of potassium (K^+, m/z 39 and 41) and calcium (Ca^+, m/z 40). The mean anion mass spectrum contains almost exclusively sulfuric acid ions, as HSO_4^- (m/z 97) and $H_2SO_4HSO_4^-$ (m/z 195). Figure 2 shows the averaged bipolar mass spectra of this particle type from two aircraft missions, namely StratoClim 2017 (18688 mass spectra) and CAFE-Africa 2018 (3310 mass spectra). During StratoClim 2017, the mass spectra were recorded using the ERICA instrument, whereas during CAFE-Africa 2018, the ALABAMA instrument was flown. Nevertheless, the two mass spectra displayed in Figure 2 look remarkably similar. A linear correlation between the mass spectra yielded an r^2 of 0.97 for both the anions and the cations. The only difference is the detection of SiO^- (m/z 44) by ERICA during StratoClim 2017. This might be due to the additional emission of 1064 and 532 nm light of the ERICA laser in contrast to the ALABAMA laser, such that the ionization probability of Si-containing compounds is higher in the ERICA instrument than in ALABAMA.

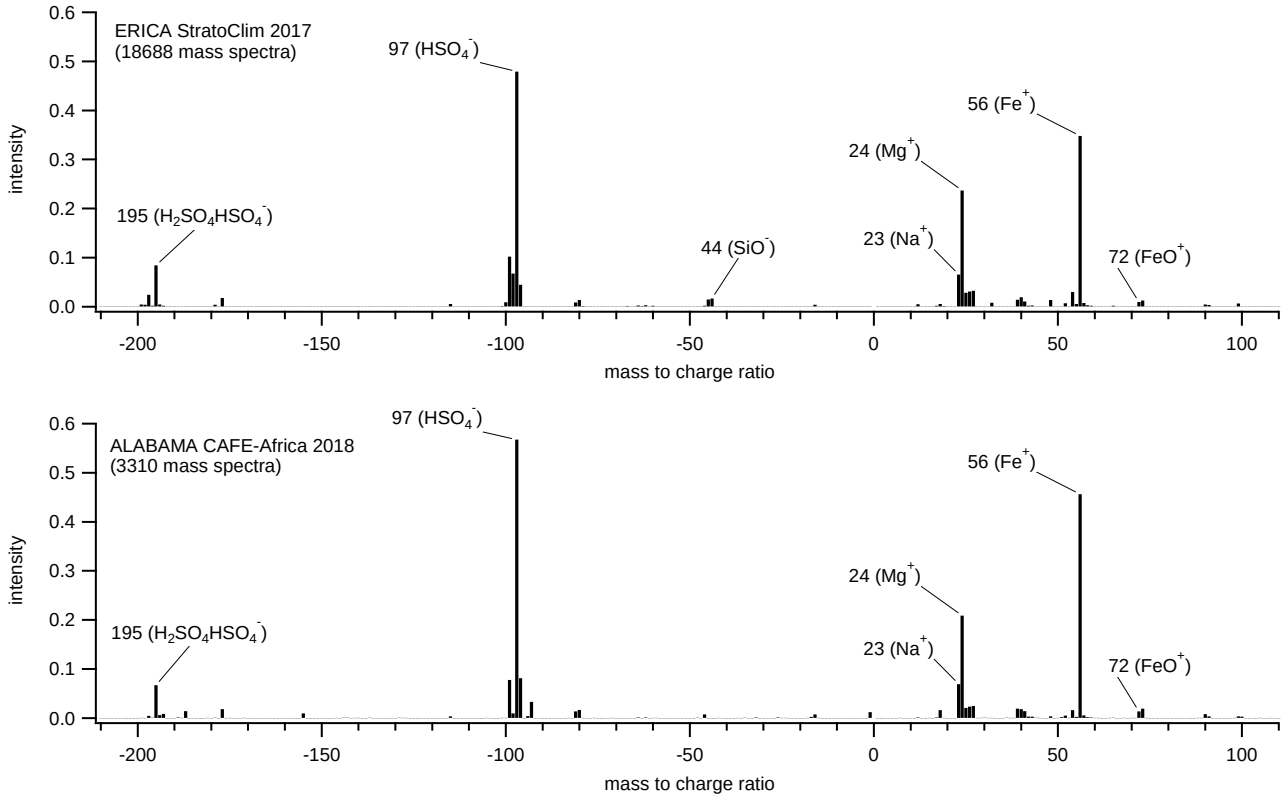

Figure 2: Mean mass spectra of clusters containing particles of which the positive mass spectra are dominated by iron (Fe^+, FeO^+) and magnesium (Mg^+). The upper panel shows the average over 18688 mass spectra recorded by the ERICA instrument during StratoClim 2017, the lower panel shows an average over 3310 ALABAMA mass spectra recorded during CAFE-Africa 2018. The two anion as well as the two cation mass spectra correlate between the instruments with $r^2 = 0.97$. The only difference is the detection of SiO^- (m/z 44) by ERICA.

Figure 3 shows the fractional abundance (number of mass spectra of this particle type relative to all recorded mass spectra), binned by altitude, potential temperature, and potential vorticity. In total, we detected 3140 particles of this type during ML-CIRRUS, 2412 during StratoClim 2016, 18688 during StratoClim 2017, 23138 during ND-MAX 2018, and 3310 during CAFE-Africa 2018 (see also Table 1). It has to be emphasized here that this fractional abundance refers to the total number of analyzed particles by ERICA and ALABAMA. Both instruments use a 266 nm laser for ablation and ionization. Pure sulfuric acid particles are not ablated and ionized at this wavelength, as was previously reported [*Thomson et al.*, 1997; *Murphy*, 2007] and also validated by laboratory measurements with ERICA. Thus the fraction of the iron and magnesium particle type given here represents an upper limit, because pure sulfuric acid particles are not taken into account. This is discussed in more detail in Section 3.5.

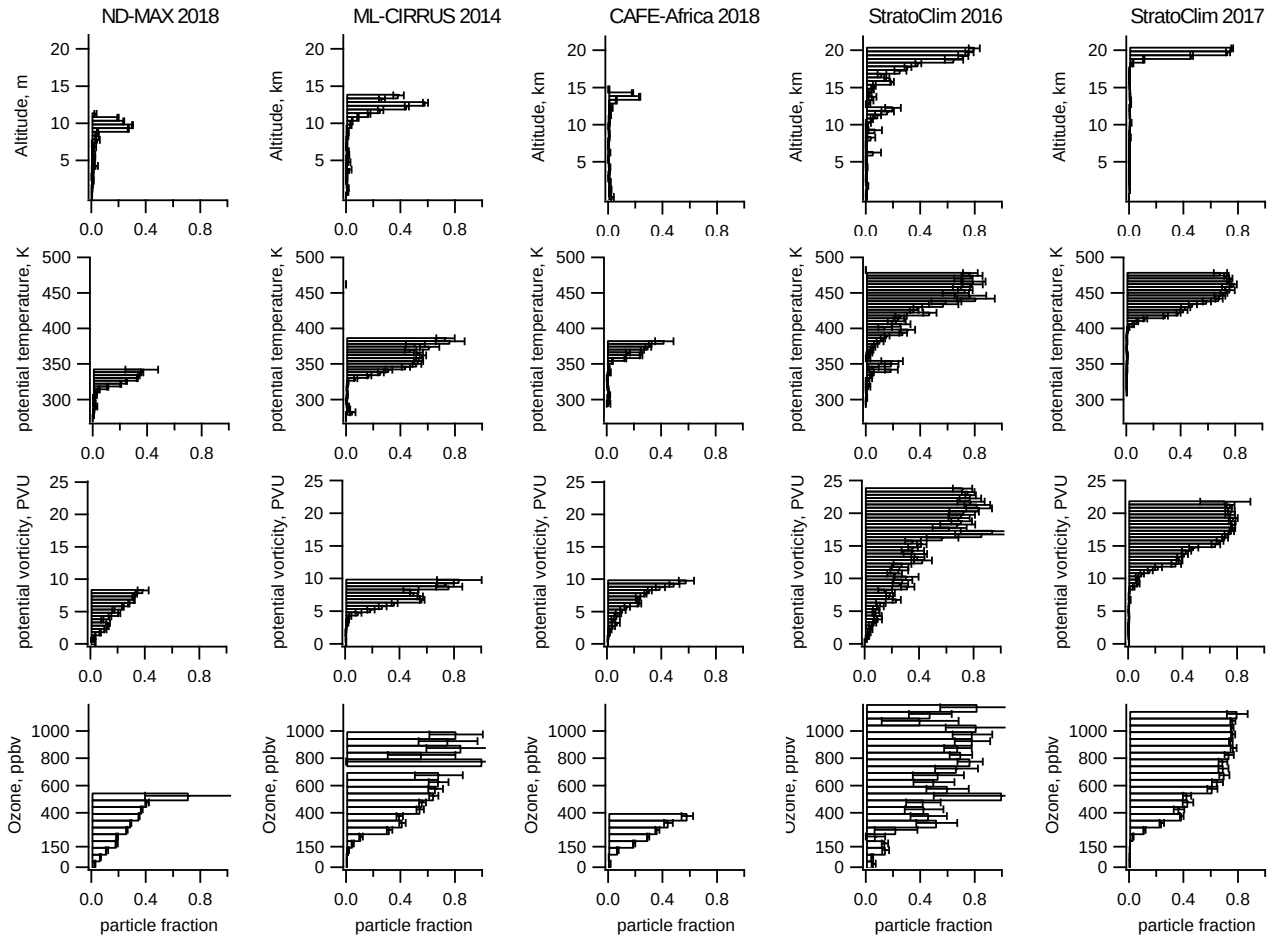

Figure 3: Fractional abundance of particles with cation spectra dominated by magnesium and iron ions. Upper row: as function of geometric altitude; second row: as function of potential temperature; third row: as function of potential vorticity (PV). The vertical profiles from the different); forth row: as function of ozone mixing ratio The missions are not sorted in chronological order but from low potential temperature (leftmost column) to high potential temperature range (rightmost column).

During these five aircraft missions, the fraction of this particle type was found to be highest in the upper flight levels (upper row in Fig. 3), reaching 0.6 at the highest flight altitudes. Very similar

values were reported by *Murphy et al.* [2014] for particles with the same ion signals in the stratosphere. The potential temperature and potential vorticity graphs (second and third rows) show that the high fractional abundance also corresponds to high values of potential temperature and potential vorticity, indicating that the measurements showing the high fractional abundance of this particle type were taken in the stratosphere. The tropopause as the boundary between tropopause and stratosphere is defined via the temperature lapse rate, but potential vorticity has been found to serve as a good indicator for the dynamical tropopause in the extratropics [*Hoskins et al.*, 1985; *Gettelman et al.*, 2011]. The threshold value used to separate the stratosphere from the troposphere in the extratropics is typically 2 PVU (potential vorticity units, 1 PVU = 10^{-6} m^2 s^{-1} K kg^{-1}, e.g., *Holton et al.* [1995]), whereas this threshold value increases up to 5 PVU in the subtropics [*Kunz et al.*, 2011]. Here we find that the increase of this particle type fraction occurs at about 2 PVU during ND-MAX/ECLIF-2, StratoClim 2016 and CAFE-Africa, at 4 PVU during ML-CIRRUS, and at 8 PVU during the tropical mission StratoClim 2017, where PV is not well suited to define the tropopause level. Therefore in the tropics a potential temperature of 380K is used instead of PV to define the tropopause. Notably during Stratoclim 2017, which took place over the AMA, the increase of the iron and magnesium containing particle fraction is found at 400 K, which is consistent with the high tropopause over the AMA.

The fraction of this particle type reaches up to more than 80 % for the highest potential vorticity or potential temperature levels during each individual mission. In the lowest row of Figure 3, ozone is used as the vertical coordinate. Here, the increase of the particle fraction starts above an ozone mixing ratio of about 150 ppbv, indicating the chemical tropopause.

The five aircraft missions were conducted in different geographical locations, such that the latitude dependence of the tropopause height causes the differences in the altitude and potential temperature profiles, as discussed in the next section.

3.2 Latitudinal distribution

The different tropopause altitudes observed during the individual missions are due the fact that the height of the tropopause is a function of latitude. The tropical tropopause corresponds to an isentropic surface at a potential temperature level of about 380 K [*Holton et al.*, 1995], corresponding to a geometric altitude of about 17 km [*Fueglistaler et al.*, 2009]. In the extratropics, the isentropes are crossing the dynamical tropopause which lies here between 2 and 5 PVU. At polar latitudes the tropopause height is typically around 8 km [*Wilcox et al.*, 2012].

To combine all data from the five aircraft campaigns, we binned all particles (in total 338354) by latitude and potential temperature, using 3° bins for latitude and 20 K bins for potential temperature. The same was done for the iron and magnesium-dominated particle type (in total 50688). Then we calculated the particle fraction of the magnesium-dominated particle type for each bin. Only bins containing more than 10 particles were considered. The result is shown in the upper panel of Figure 4 (separated graphs for the individual missions are given in the supplement in Figure S6). We also inserted the thermal tropopause from the ECMWF data set, binned into 4 degree latitude bins. The median thermal tropopause is given by the thick dashed line and the 25% and 75% quartiles by the gray shaded area. Additionally, a 2 PVU and a 5 PVU surface are shown by the thin dashed lines, indicating the dynamical tropopause (2 PVU at mid latitudes and 5 PVU in the subtropics). For this, we took all potential temperatures where the potential vorticity ranged between 1.5 and 2.5 PVU (4.5 and 5.5 PVU, respectively) and binned these values into 4 degree latitude bins.

The same procedure, for the particle fraction, the thermal tropopause and the dynamical tropopause, was used to bin the data as a function of equivalent latitude (lower panel of Figure 4). The equivalent latitude of an air parcel is calculated by transforming the contour having the same potential vorticity and potential temperature into a circle centered at the pole. The latitude enclosing this circle is then defined as the equivalent latitude. Since potential vorticity is conserved under adiabatic processes, equivalent latitude can be used to account for reversible adiabatic tracer transport by e.g. planetary waves [*Hegglin et al.*, 2006; *Hoor et al.*, 2010; *Krause et al.*, 2018].

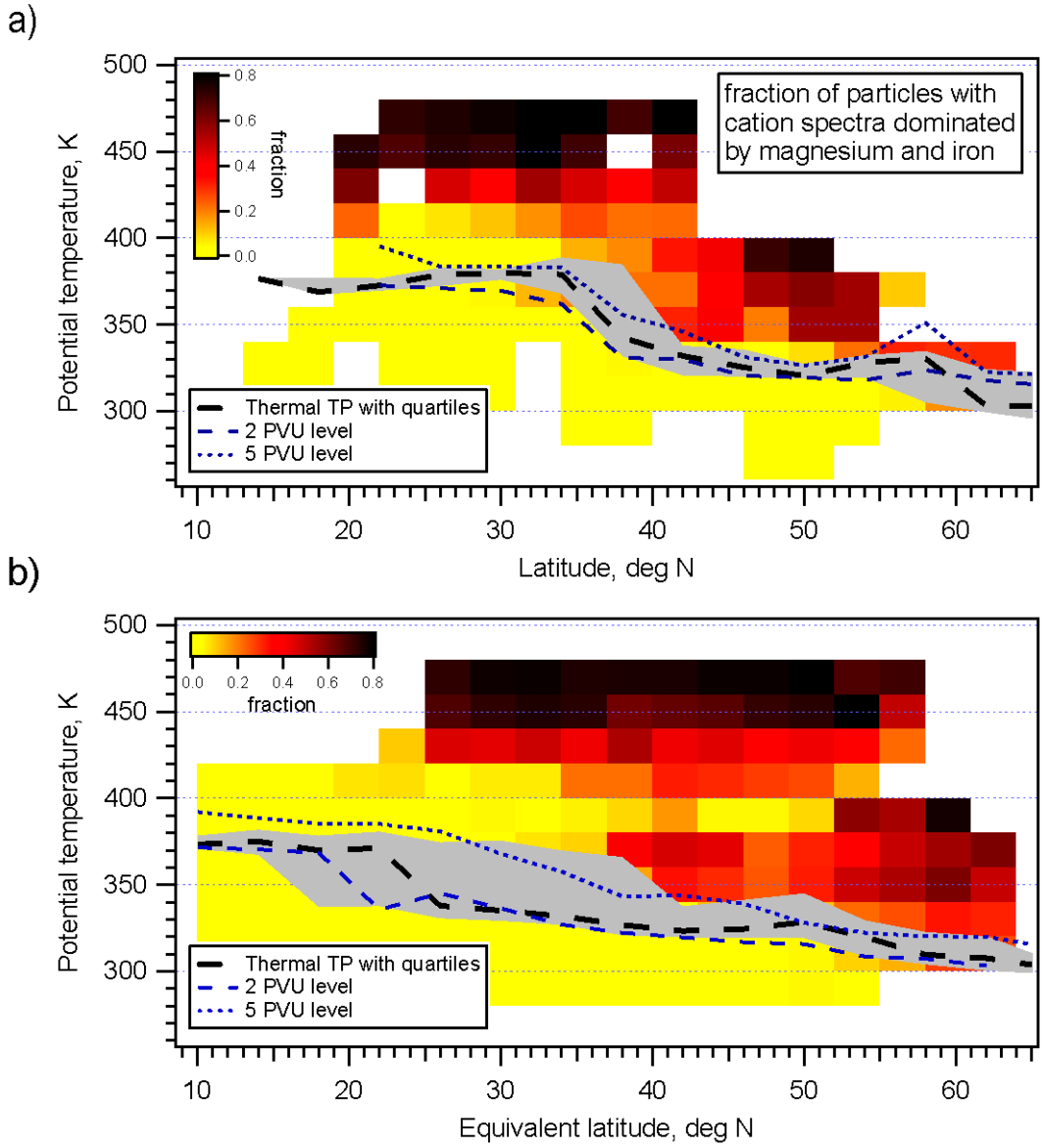

Figure 4: Fractional abundance of particles with cation mass spectra dominated by magnesium and iron ions as a function of potential temperature and latitude (upper panel) and as a function of potential temperature and equivalent latitude (lower panel). The data of all five UTLS aircraft missions have been merged for this figure (in total 338354 analyzed particles). Also shown is the median thermal tropopause (from ECMWF) along with quartiles and two dynamical tropopause levels (2 PVU and 5 PVU).

In geographical latitude space (Fig. 4 a), the thermal tropopause reaches the 380 K level at 38°N and remains between 370 and 380 south of 38°N. At mid-latitudes, the tropopause height decreases until it reaches 300 K above 60°N. In equivalent latitude space (Fig. 4 b), the thermal tropopause shows more variation (larger interquartile range), especially between 20 and 40°N.

Both plots in Figure 4 show that the fraction of the iron and magnesium-dominated particles increases in high and middle latitudes very close to the position of the tropopause, but not in the tropics. In theta-latitude space (Fig. 4 a), the particle fraction remains as low as in the troposphere between the tropopause (around 370 - 380 K) and 400 K at latitudes below 30°N. In theta-equivalent latitude space (Fig. 4 b), this effect is even more pronounced: Below 35°N equivalent latitude, the area between the

tropopause and 420 K shows a very low fraction of the iron and magnesium-dominated particles. This corresponds to the PV profile of the StratoClim 2017 data from Figure 3, because the stratospheric tropical data in Figure 4 are dominated by the StratoClim 2017 data set. In the AMA which dominated the geographical region of StratoClim 2017 during the time of the campaign, the air masses are transported upwards between about 360 K and 460 K [Ploeger et al., 2017; Vogel et al., 2019]. The observation that the fraction of the iron and magnesium-dominated particle type increases only above the extratropical tropopause layer or mixing layer [Hoor et al., 2002; Hoor et al., 2004; Pan et al., 2004], i.e. 30 K above the tropopause (Fig. 4 a), indicates that the source for this particle type must be in the stratosphere, because otherwise, the upwelling air masses in the AMA would contain this particle type also at lower potential temperatures. In the stratosphere, the widespread occurrence of high fractions of this particle type over a broad range of latitudes (Fig 4a) and equivalent latitudes (Fig 4b) above 440 K shows that this particle type is very homogeneously distributed in the stratosphere. This indicates that isentropic mixing between high and low latitudes is very effective above 440 K.

3.3 Interpretation as meteoric particles

From the previous discussion we concluded that the source of this particle type is likely found in the stratosphere. The capacity to record bipolar mass spectra of single particles allows to show that each particle whose cation mass spectrum is dominated by Mg and Fe contains sulfuric acid but no other frequently observed anions like NO^-, NO_2^-, CN^-, or CNO^-. We therefore conclude that the particles we observe consist of meteoric material dissolved in sulfuric acid. This interpretation follows the argumentation by *Murphy et al.* [1998] and *Cziczo et al.* [2001] who measured stratospheric particle composition using a similar laser ionization mass spectrometer (PALMS) on board the WB-57F high altitude research airplane between 5 and 19 km altitude. Further data from airborne single particle mass spectrometry [*Cziczo et al.*, 2001; *Cziczo et al.*, 2004; *Murphy et al.*, 2007; *Murphy et al.*, 2014] as well as laboratory measurements with reference meteoric samples and artificial meteorite particles supported this conclusion [*Cziczo et al.*, 2001]. Our cation mass spectra (Figure 2) show a very similar ion signature as the cation mass spectra from stratospheric particles, dissolved meteorites and artificial meteorite particles presented in *Cziczo et al.* [2001]. The finding that Si is observed to a much lesser degree that expected from meteoric composition (roughly equal amounts of Fe, Mg, and Si) was explained by *Cziczo et al.* [2001] and *Murphy et al.* [2014] by the low solubility of SiO_2 in H_2SO_4. Thus, Si is assumed to present as a solid inclusion and is thereby less efficiently ionized compared to the other metals that are dissolved in H_2SO_4.

Other sources for this particle type, like aircraft or rocket exhaust, uplifting of particles (e.g. desert dust) from the Earth's surface and volcanic injection, can be ruled out: The majority of aircraft traffic does not occur at such high altitudes at which the meteoric particles were observed in the tropical stratosphere. Rocket exhaust can be ruled out because the dominating metal in rocket exhaust particles is expected to be Al [*Voigt et al.*, 2013]. Single particle mass spectrometric measurements of rocket exhaust plumes showed ions of chlorine and oxygen, of metals like Al, Fe, Ca, Na, and K, but not of magnesium [*Cziczo et al.*, 2002]. Furthermore, rocket exhaust plumes would hardly lead to the observed uniform and wide geographical distribution of the particles. Volcanic aerosol particles have been measured in the tropopause region and lowermost stratosphere after eruptions of Kasatochi and Sarychev [*Andersson et al.*, 2013]. These data show that volcanic aerosol contains a larger weight percentage of carbonaceous material than of ash, which is not reflected by our data. Furthermore, volcanic ash particles indeed contain a number of elements that are abundant in meteorites, like Fe, Si, Ca, K, but additionally also elements that are characteristic for crustal material like titanium which was not observed in our mass spectra. As crustal material that can occur as particles in the troposphere (like soil dust or desert dust) contains the same elements like the stratospheric particles we observed (e.g., Na, Mg, Al, K, Fe), interferences with dust particles in the troposphere might be possible, although the ions FeO^+ and $FeOH^+$ (m/z 72, 73) have not been observed in single particle spectra of mineral dust [*Gallavardin et al.*, 2008]. In the tropical regions, uplifting of particles from the troposphere into the

stratosphere occurs especially in the AMA [*Randel et al.*, 2010; *Pan et al.*, 2016; *Yu et al.*, 2017] and might also carry dust particles into the stratosphere. However, to explain the stratospheric abundance of the observed Fe- and Mg-rich particle type, this particle type would need to be found already during the upward transport in the AMA, which is clearly not the case (Figure 4). The mean mass spectra and the vertical profiles of one frequently observed particle type containing Fe, K, Na, as well as smaller signals of Mg and Ca, is shown in Figure 5. This particle type was occasionally observed in the stratosphere (ML-CIRRUS, StratoClim 2017, CAFE-Africa), but in general occurred mainly in the troposphere. We interpret this particle type as an internal mixture of mineral dust, sea spray, sulfate, and nitrate, due to Na^+, K^+, and Fe^+ cations and chlorine ($^{35}Cl^-$, $^{37}Cl^-$), nitrate (NO^-, NO_2^-), and sulfate (SO^-, SO_2^-, SO_3^-, HSO_4^-) anions. It was therefore not included in the meteoric data set discussed in this paper. The reason why such particles were found in the stratosphere during ML-CIRRUS is presumably an outbreak of Saharan dust and its transport towards Europe during the time of the campaign [*Weger et al.*, 2018]. During StratoClim 2017 and CAFE-Africa the vertical uplifting can most likely be explained by the Asian and African monsoon systems.

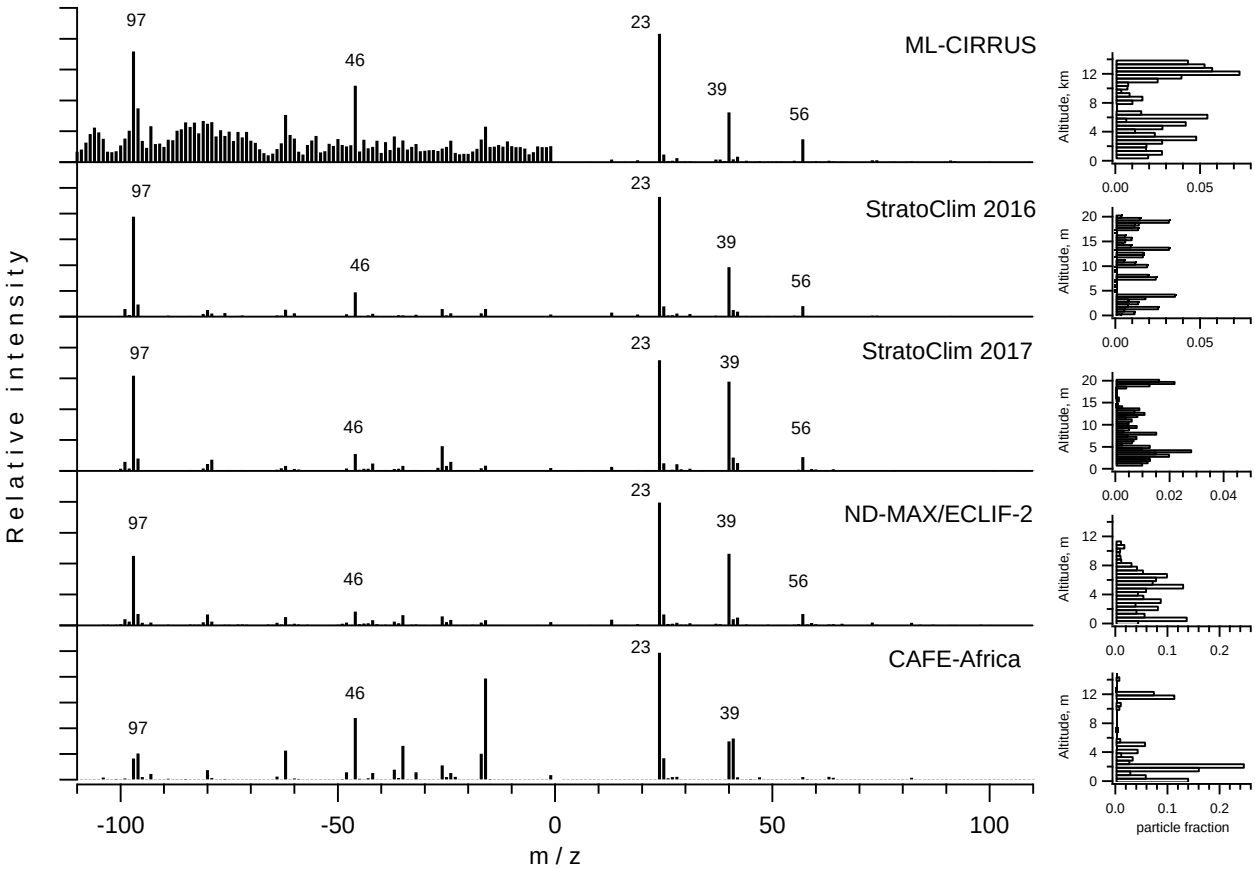

Figure 5. Mean mass spectra and vertical profiles of a particle type containing Na, K, and Fe, with smaller amounts of Mg and Ca. This type, which was observed in all five high altitude aircraft missions, does not belong to the meteoric particles, although it was sometimes observed at higher altitudes. It can be interpreted as mineral dust, internally mixed with sea spray and secondary inorganic compounds (nitrate, sulfate).

3.4 Size-resolved fraction of meteoric particles

Both particle mass spectrometers used here (ALABAMA and ERICA) determine the particle velocity in the vacuum chamber which by laboratory calibration can be converted into the vacuum

aerodynamic diameter (d_{va}, *DeCarlo et al.* [2004]) of each individual particle. To obtain the size distributions shown in Figure 6, we used logarithmically equidistant size bins between 100 and 2000 nm (ML-CIRRUS) and 100 and 5000 nm (StratoClim). These size distributions represent the product of instrument efficiency (inlet transmission, particle detection and ablation rate) and the ambient particle size distribution. Differences between the measurements with ALABAMA during ML-CIRRUS and ERICA during StratoClim 2017 are therefore mainly due to such instrumental parameters. The particle sizes were separated between tropospheric (PV < 2 PVU) and stratospheric (PV > 4 PVU) conditions. In both data sets, the tropospheric particles tend to be smaller than the stratospheric particles. Fig. 6 also depicts the size distribution of the meteoric particles, and in the lower panel the ratio between the meteoric particles (also selected for stratospheric conditions) and all stratospheric particles. It turns out that the fraction of meteoric particles is smallest in the lower size range for both campaigns: In the ML-CIRRUS data set, the fractional contribution increases from about 0.2 at 250 nm to about 0.5 at 300 nm and remains almost constant at 0.5 up to 1000 nm. The StratoClim data set extends both to smaller and larger sizes and contains a larger number of particles. Here it can clearly be seen that the fraction of meteoric particles is zero at 200 nm, although stratospheric particles are detected even below 200 nm. The meteoric fraction rises to 0.7 at 450 nm and decreases above that size, down to 0.2 at about 1600 nm. Above that size, only one meteoric particle was detected, although in total 253 stratospheric particles were measured between 1600 and 4400 nm. Thus, the meteoric fraction appears to decrease down to zero above $d_{va} \approx 1600$ nm. This finding is similar to the data shown by *Murphy et al.* [2014] who found a maximum of meteoric particles at diameters of around 600 – 700 nm and a decrease down to zero above $d_{va} = 1$ µm. However, the fraction of meteoric particles below 600 nm is markedly higher in our data set. The finding that a high fraction of non-meteoric stratospheric particles is found between 200 and 300 nm during StratoClim 2017 is most likely due to the upwelling of air in the AMA and the associated vertical transport of particles from the troposphere. However, a more detailed analysis of the AMA influence on stratospheric aerosol will be discussed in a separate publication. The observed size range of the meteoric particles (between about 250 and 1500 nm indicates that their sedimentation may play an important role for the downward transport of meteoric material through the stratosphere (see Section 4). Once the meteoric aerosol material has reached altitude levels near the tropopause, its rapid removal out of the stratosphere due to cross-tropopause exchange and cloud formation processes is likely.

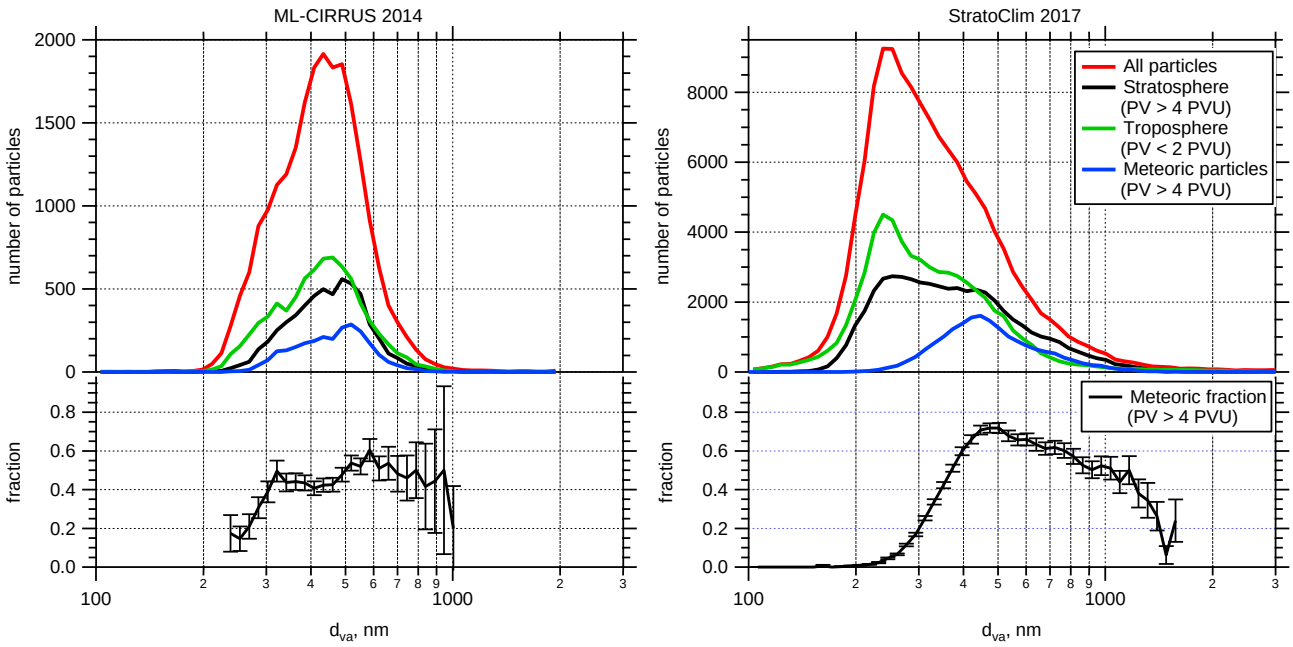

Figure 6. Number of analyzed single particles as a function of particle size (vacuum aerodynamic diameter, d_{va}) measured during ML-CIRRUS 2014 and StratoClim 2017. Upper row: Absolute number of counted particles per size bin. Lower row: Fraction of meteoric particles in the stratosphere (PV > 4 PVU).

3.5 Absolute number concentration

It is difficult to estimate an absolute number concentration of particles containing meteoric material from the measured particle fraction with a laser ablation mass spectrometer. The main reason is that pure sulfuric acid particles are not ablated and ionized by a laser with a wavelength of 266 nm, because sulfuric acid has a very low absorption cross section for wavelengths larger than about 190 nm up to visible light [*Thomson et al.*, 1997; *Burkholder et al.*, 2000; *Murphy*, 2007]. Thus, the fraction of particles containing meteoritic material will be overestimated if pure sulfuric acid aerosol particles existed in the air.

The hit rate of the mass spectrometer, which is defined here as the number of acquired mass spectra per time unit divided by the number of laser shots per time unit, can be used to estimate the number of missed particles. Our data show that the hit rate in the stratosphere is generally lower than in the lower troposphere. Two examples (for ML-CIRRUS and CAFE-Africa) are shown in Figure S8 in the supplement. The maximum achieved hit rate in the troposphere was about 0.8 during CAFE-Africa, whereas the averaged hit rate in the stratosphere was about 0.2, thus, lower by a factor of 4. A similar decrease, albeit at lower absolute values of the hit rate, was observed during ML-CIRRUS. If we assume that the decrease of the hit rate in the stratosphere is only due to the abundance of pure sulfuric acid particles that were not ablated, we can estimate the absolute number of meteoric particles by dividing the fraction measured by the mass spectrometer by a factor of 4 (to account for the hit rate decrease) and multiplying by the total particle number concentration measured by an independent absolute particle counting (and sizing) instrument [*Qin et al.*, 2006; *Gunsch et al.*, 2018; *Froyd et al.*, 2019].

For ML-CIRRUS, we used the optical particle spectrometer "Sky-OPC" (Grimm 1.129). The nominal lower cut-off diameter (manufacturer calibrated with PSL particles) is 250 nm. To account for the refractive index of stratospheric particles, we performed Mie calculations for refractive indices between 1.43 and 1.45 [*Yue et al.*, 1994]. This resulted in a lower cut-off diameter for stratospheric aerosol particles of 285 nm in diameter (supplement, Figure S11). The size distributions in Figure 6 show that for ML-CIRRUS the meteoric fraction is approximately constant between vacuum aerodynamic diameters greater than 300 nm. This value translates into a volume equivalent diameter (d_{ve}) of about 180 nm, assuming a density of the lower stratospheric particles of 1.7 g cm^{-3} [*Yue et al.*, 1994]. We also note that the size distribution showed that 99.8 % of all particles counted by the OPC in the stratosphere are below 1000 nm. Thus, we can assume a constant fraction of meteoric particles for the particles counted by the OPC and therefore multiplying the binned meteoric particle fraction (divided by 4) from Figure 3 with the binned number concentration measured by the OPC should give an estimation of the absolute concentration of meteoric particles larger than 280 nm for the mid-latitude data set from ML-CIRRUS 2014.

For StratoClim 2017, we used data recorded by the UHSAS (DMT Inc.). According to the size distribution of meteoric particles in Figure 6, the meteoric particles fraction reaches about 50% of its maximum fraction at 340 nm (d_{va}). This translates into a volume equivalent diameter (d_{ve}) of 200 nm (assuming the same density for stratospheric aerosol as above). Mie calculations using the refractive index range from 1.43 to 1.45 (Figure S11) yield that a lower size limit of 180 nm (PSL calibration) corresponds to a d_{ve} of 200 nm for stratospheric aerosol. We therefore used the integrated particle number concentration between 180 nm and 1000 nm (PSL calibration), multiplied this with the fraction of meteoric particles from Figure 3 and divided by 4 to account for the hitrate. This procedure gives an estimation of the absolute concentration of meteoric particles larger than 200 nm for the tropical data set from StratoClim 2017.

Figure 7 shows the total particle concentrations for the two missions named above as a function of altitude, potential temperature and potential vorticity for the upper troposphere and lower stratosphere. The 6 second raw data are shown along with binned mean, median, and quartiles. The

calculated meteoric particle concentrations are shown as binned median values with quartiles. The highest absolute number concentrations of meteoric particle range around 0.2 cm^{-3} (referring to ambient pressure and temperature). During StratoClim 2017 (conducted at tropical latitudes) these values are reached above 20 km, Θ = 450 K, and 17 PVU. During ML-CIRRUS, values of 0.2 cm^{-3} are only reached at PV > 9 PVU, whereas in altitude and potential temperature coordinates the concentrations reach only 0.1 cm^{-3}. Nevertheless, the absolute range of meteoric particle concentration is very similar for both data sets, although the calculation of the meteoric particle concentration relies on different size ranges of the optical instruments and is based on several assumptions, as detailed above.

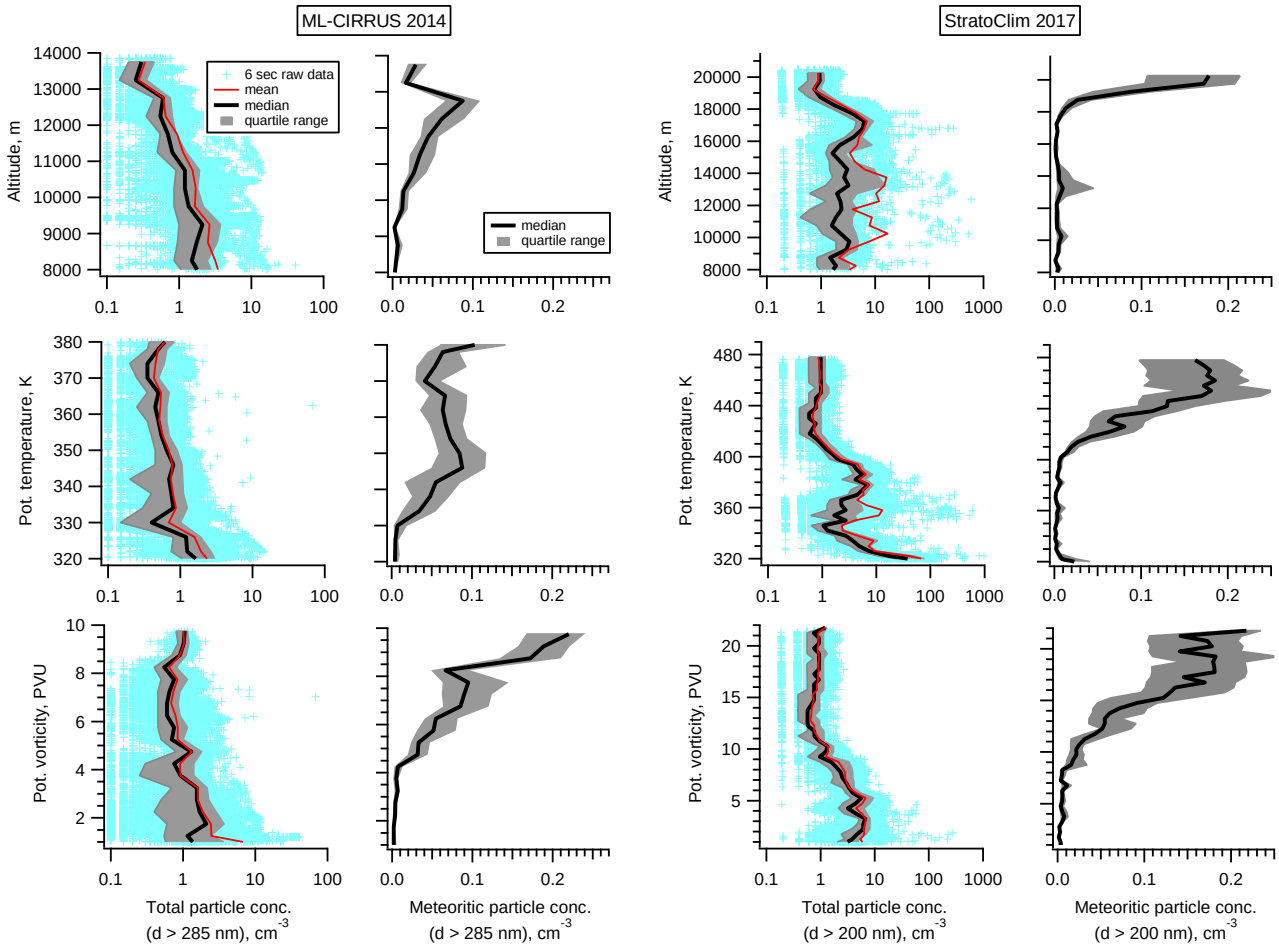

Figure 7. Total particle number concentrations measured during ML-CIRRUS 2014 (d_{ve} > 285 nm, first column) and StratoClim 2017 (d_{ve} > 200 nm, third column) along with calculated number concentrations of particles containing meteoric material (second column: ML-CIRRUS 2014; fourth column; StratoClim 2017). Data are shown for the upper troposphere and lower stratosphere (Altitude > 8 km, Θ > 320 K, PV > 1 PVU) measured during ML-CIRRUS. Light blue markers: 6 second raw data; red line: mean; black line: median; grey area: quartiles (25% and 75%).

3.6 Transport mechanism for cross-tropopause exchange

To investigate the downward transport of meteoric particles through the tropopause into the troposphere, we use the tracer-tracer correlation of ozone as a stratospheric tracer and water vapor as a tropospheric tracer. Tracer-tracer correlations have been widely used to identify the mixing layer

between troposphere and stratosphere [*Fischer et al.*, 2000; *Hoor et al.*, 2002; *Pan et al.*, 2004; *Marcy et al.*, 2007; *Gettelman et al.*, 2011; *Krause et al.*, 2018]. It is more common to use carbon monoxide as a tropospheric tracer, but because it was not measured during ML-CIRRUS, we use water vapor for which the applicability to serve as a tropospheric tracer in tracer-tracer correlations has been shown by *Gettelman et al.* [2011], *Pan et al.* [2014] and *Heller et al.* [2017]. High ozone values indicate stratospheric air (vertical branch), high H_2O values tropospheric air (horizontal branch). Figure 8 shows the tracer-tracer correlations between ozone and H_2O for ML-CIRRUS, StratoClim 2017, ND-MAX/ECLIF-2, and CAFE-Africa. The data coverage of O_3 and H_2O during StratoClim 2016 was not sufficient (see supplement, Fig S10). The left panels show all data from the trace gas measurements, color coded by equivalent latitude.

The mid-latitude data from ML-CIRRUS (top left graph of Figure 8) show a clear separation between air masses of mid latitude and tropical origin: The mixing lines, indicating irreversible mixing between the troposphere and the stratosphere have equivalent latitudes > 30°N, whereas the green colored data points that correspond to tropical air masses (equivalent latitude < 30°N) do not show such mixing. The top right graph shows the H_2O and O_3 data for all sampled particles (gray) and for all meteoric particles (black). As expected, the density of black data points is highest in the stratospheric branch of the tracer-tracer correlation. Mixing between extratropical stratospheric and tropospheric air is indicated by mixing lines with equivalent latitudes > 30°N, connecting regions of elevated extratropical and low stratospheric H_2O values. Isentropic mixing between dry air which passed the Lagrangian cold point (and therefore exhibits H_2O mixing ratios < 6 ppmv) and higher latitudes is indicated by the vertical branch starting at O_3 mixing ratios < 150 ppbv, connecting the dry upper tropical troposphere with the stratosphere.

In the StratoClim 2017 data set (second row) no mixing lines were observed. Only very few meteoric particles are observed in the tropospheric branch of the O_3-H_2O plot (below 100 ppbv O_3), showing that downward mixing of meteoric particles from the stratosphere does not occur in the upwelling tropical air masses of the AMA (see also Fig. 4).

The data sets of ND-MAX/ECLIF-2 and CAFE-Africa appear similar in this tracer-tracer correlation, although the geographic latitudes and seasons of the two campaigns were very different. In both missions, highest observed O_3 values are 400 – 500 ppbv, and the equivalent latitudes reach up to 60 – 70°N in the stratosphere. Both data sets show a high degree of stratosphere-troposphere mixing, as can been seen from the higher H_2O mixing ratios at O_3 levels between 100 and 200 ppbv, corresponding to the mixing lines observed during ML-CIRRUS. Along these mixing lines, meteoric particles are frequently observed, even at tropospheric altitudes where water vapor mixing ratios of > 1000 ppmv are reached.

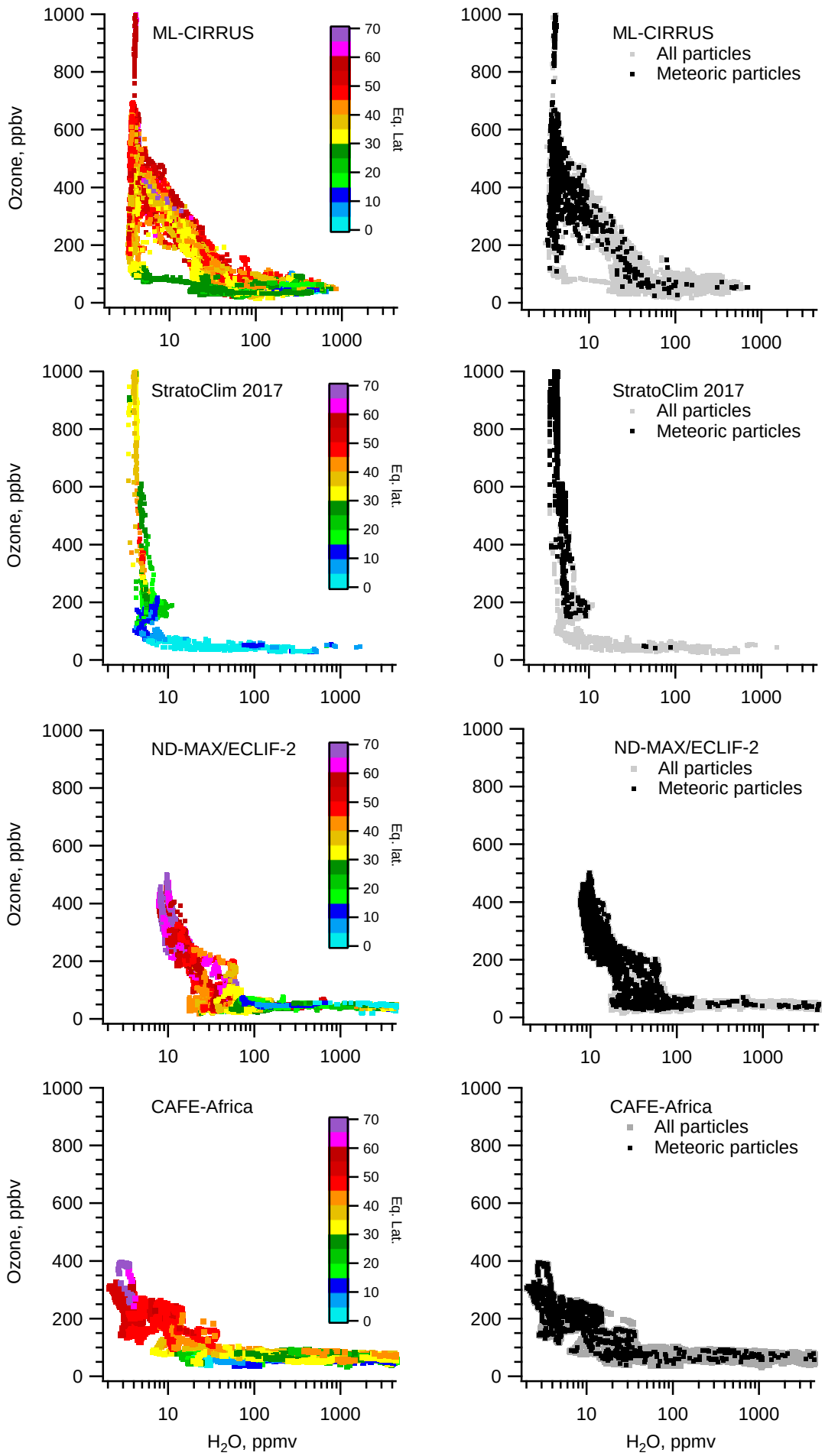
ML-CIRRUS
Eq. Lat
All particles
Meteoric particles
StratoClim 2017
Eq. lat.
ND-MAX/ECLIF-2
CAFE-Africa
Ozone, ppbv
H_2O, ppmv

644

Figure 8. Ozone mixing ratio as stratospheric tracer versus water vapor mixing ratio as tropospheric tracer, for ML-CIRRUS (upper row), StratoClim 2017 (second row), ND-MAX/ECLIF-2 (third row), and CAFE-Africa (bottom row). Left: All data, color-coded with equivalent latitude. Right: O_3 and H_2O for the times when particle mass spectra were recorded. Gray: all particles, black: meteoric particles.

3.7 Detection of particles containing meteoric material at low altitudes

Figure 8 showed that particle containing meteoric material are transported downwards through stratosphere-troposphere exchange and are therefore also present in the troposphere, albeit at low concentrations and low number fractions. We used two data sets from lower altitudes to estimate the occurrence of this particle type in the middle and lower troposphere. These are the abovementioned NETCARE data set (Canadian Arctic, summer 2014) that contains aircraft-based ALABAMA data up to 3 km altitude [*Köllner et al.*, 2017] and a mountain-top data set from the Jungfraujoch station at 3600 m altitude in winter 2017. In both data sets the relative number of meteoric particles was very low, such that an automated cluster algorithm would not find this particle type unless the prescribed number of cluster would be set to very high values. Thus, we used the most prominent mass spectral features from this particle type as observed in the stratosphere (Figure 2) and scanned the two low-altitude data sets for these marker peaks. The criteria included the presence of ^{24}Mg, ^{25}Mg, ^{26}Mg, ^{54}Fe, ^{56}Fe, the absence of Cl (to exclude sea spray) and signal intensity of m/z 39 smaller than that of m/z 41. The latter was introduced to minimize the influence of potassium from other sources, especially dust. By varying these search criteria, different numbers of mass spectra with similar average mass spectra were obtained, such that the absolute amount of meteoric particle at low altitude is highly uncertain. Figure 9 shows the averaged mass spectra matching the criteria given above. The spectra correspond very well to the spectra sampled in the stratosphere (Figure 2). A higher contribution of m/z 18 (NH_4^+), especially in the Jungfraujoch spectra indicates a higher degree of neutralization of the sulfuric acid by ammonia in the troposphere than in the stratosphere. During NETCARE, six out of about 10000 particle mass spectra matched the criteria. By changing the criterion for potassium to an absolute upper intensity threshold, the number of spectra was reduced to three. Thus, the fraction of meteoric particles found in the summer Arctic lower troposphere can be estimated to be around 0.025 – 0.05%. In the free tropospheric data set obtained in winter at the Jungfraujoch, about 4100 spectra (out of more than 765000) matched the criteria, corresponding to 0.5%. Also here, by varying the criteria the percentage varies between 0.2 and 1%. This range is clearly larger than that in the Arctic summer, but it has to be kept in mind that the Jungfraujoch data set was obtained at 3600 m altitude, whereas the measurements during NETCARE only reached up to 3000 m. In winter the Jungfraujoch station is mainly located in the free troposphere (over 60% of the time, see *Bukowiecki et al.* [2016]), such that the influence of boundary layer particles is low. In contrast, the aerosol in the summer Arctic during NETCARE was to a large degree influenced by particles from marine biogenic origin [*Köllner et al.*, 2017]. Backtrajectory calculations for the Jungfraujoch data set showed that the fraction of detected meteoric particles was higher during times when the air masses experienced higher altitudes and higher latitudes during the 5 days before the measurements (Supplement, Section 9 and Figure S12). Additionally, the fraction of meteoric particles followed the time trend of the ozone mixing ratio (Figure S12), confirming the stratospheric origin. Overall, this shows that the meteoric material immersed in stratospheric sulfuric acid aerosol reaches the lower troposphere from where it will be removed by wet removal (rain-out, wash-out), thereby finally reaching the Earth's surface. This is confirmed by a number of studies that reported the detection of meteoric material in ice cores samples from Greenland [*Gabrielli et al.*, 2004; *Lanci et al.*, 2012] and Antarctica [*Gabrielli et al.*, 2006].

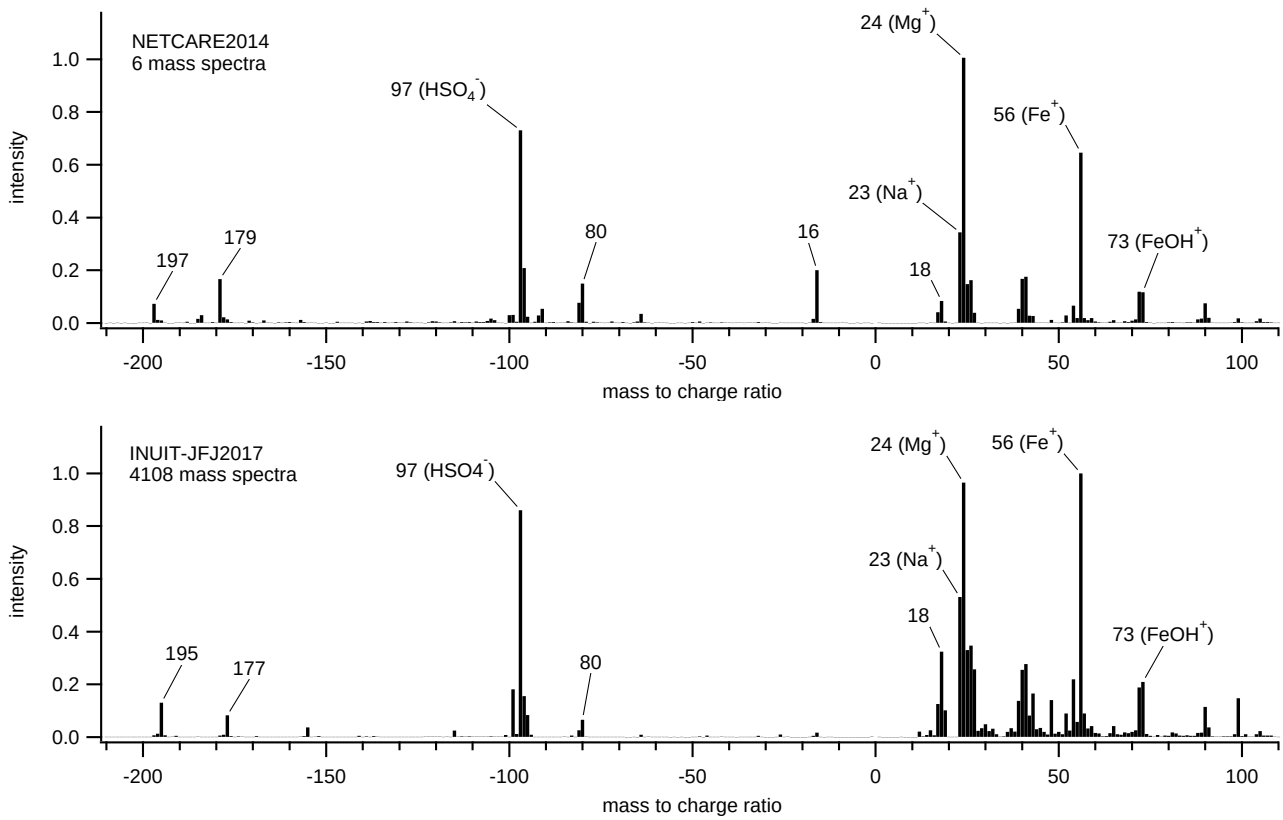

Figure 9: Mass spectra from low altitudes (NETCARE, Canadian Arctic, summer 2014, up to 3 km; Jungfraujoch, Switzerland, winter 2017, 3600 m) showing meteoric signatures.

4 Discussion and conclusion

In this study we present stratospheric single particle mass spectrometer data from five aircraft-based campaigns, covering a wide range of northern hemispheric latitudes (15°N – 68°N) and seasons (winter, spring, summer). In all data sets a distinct particle type characterized by iron and magnesium was observed in the stratosphere. The observed distribution as function of potential temperature and potential vorticity suggests that the source of this particle type is in the stratosphere. From previous stratospheric data [*Mossop*, 1965; *Murphy et al.*, 1998; *Cziczo et al.*, 2001; *Murphy et al.*, 2014], meteoric composition data [*Lodders and Fegley Jr.*, 1998; *Rapp et al.*, 2012; *Plane et al.*, 2015], and theory of meteoric ablation and fragmentation [*Plane*, 2003; *Carrillo-Sánchez et al.*, 2016; *Subasinghe et al.*, 2016], it was concluded that this particle type represents meteoric material dissolved in sulfuric acid droplets, in particular in the Junge layer.

It was previously widely assumed that downward transport of MSP particles from the mesosphere into the stratosphere occurs most efficiently in the polar vortex [*Curtius et al.*, 2005; *Megner et al.*, 2008; *Plane*, 2012; *Murphy et al.*, 2014; *Weigel et al.*, 2014; *Kremser et al.*, 2016]. One would therefore expect to find a higher abundance of meteoric particles in the lower stratosphere at high latitudes during late winter and early spring than at low latitudes during other seasons. This is not confirmed by our observations: Although two mid-latitude campaigns (ML-CIRRUS and ND-MAX/ECLIF-2) were conducted between January and April, we observe the same fraction of meteoric particles in the lower stratosphere (Figure 3) during all campaigns, regardless of latitude and season.

It is therefore much more likely that the meteoric particles observed in the lower stratosphere originate directly from the stratospheric Junge layer. Satellite observations with the CALIOP lidar instrument have shown that the lower edge of the Junge layer lies between 450 and 500 K potential temperature for latitudes between 20 and 50°N [*Vernier et al.*, 2009]. Thus, our measurements between

20 and 40°N reach up to the lower edge of the Junge layer (see Figure 4), whereas at higher latitudes and lower altitudes we assume that we observed particles that settled gravitationally from the Junge layer. This in turn means that the Junge layer particles contain meteoric material at all latitudes. We therefore conclude that meteoric material is carried by the downward branch of the Brewer-Dobson-Circulation from the mesosphere to the stratosphere, where isentropic mixing occurs within the extratropics, but also between the tropics and extratropics [*Neu and Plumb*, 1999; *Garny et al.*, 2014]. This mixing process that has been referred to as "leaky pipe" [*Neu and Plumb*, 1999] distributes the meteoric material over all latitudes. From our data we can infer that at the altitude of the Junge layer (20 – 25 km; 500 – 600 K) the meteoric material is equally distributed throughout the latitude range of about 20 to 60°N. The homogeneous distribution of the meteoric particle above 440 K (Fig. 4) confirms the concept of effective isentropic mixing. Our observations do not give a clear indication whether the detected particles containing meteoric material originate from meteor smoke particles (MSP) dissolved in Junge layer particles or from meteoric fragments (MF) or unablated interplanetary dust particles (IDP) that are coated by sulfuric acid. However, the high H_2SO_4 content of all detected meteoric particles and the uniform mass spectra suggest that MSP dissolved in sulfuric acid are the most likely particle source.

We calculated the terminal settling velocity for particles of different sizes and densities (pure H_2SO_4, $\rho = 1.83$ g cm^{-3}, and pure olivine as a surrogate for meteoric composition, $\rho = 3.30$ g cm^{-3}) as a function of altitude (for details see supplement). Between 16 and 18 km, the settling velocity ranges between 1 and 12 m/day for particles between 100 and 500 nm having the densities given above. In the AMA, air masses are transported upwards between about 360 K and 460 K with about 1.5 K/day [*Ploeger et al.*, 2017; *Vogel et al.*, 2019], corresponding to about 35 – 40 m / day. This is larger than the above calculated range, thus sedimentation is not fast enough to overcome the Asian monsoon upward motion. This explains that in the tropics we observe the increased fraction of particle containing meteoric material only 30 K above the thermal tropopause (see Figure 4) whereas in the extratropics, where no upward motion exists, we see these particles directly above the tropopause.

Our data further show that all meteoric particles contained H_2SO_4, but no other anions like nitrate or organic material. Thus, from our simultaneous cation and anion measurements we can confirm previous assumptions that Mg and Fe are dissolved in H_2SO_4 [*Murphy et al.*, 1998; *Cziczo et al.*, 2001; *Murphy et al.*, 2014]. This suggests that these particles behave like H_2SO_4 droplets in the UT with respect to cirrus formation and also in the polar stratosphere with respect to PSC formation. In general, this particle type represents a good tracer for stratospheric aerosol particles. Downward transport along mixing lines at mid-latitudes was clearly identified, but only for equivalent latitudes above 30°N. In data sets acquired in the lower troposphere this particle type was detected as well, albeit only in very minor abundance. Their size and composition (larger than 200 nm, composed mainly of H_2SO_4, most likely neutralized by ammonia in the troposphere) makes them ideal CCN, such they will be efficiently removed from the atmosphere by nucleation scavenging and wet removal and the meteoric material is by this process transported to the Earth's surface.

Acknowledgements:

This work was funded by the DFG Priority Program SPP 1294, grant SCHN1138/1-2 (ML-CIRRUS), by the European Research Council (ERC), EU FP7/2007–2013, Projects No. 603557 (StratoClim), and No. 321040 (EXCATRO). StratoClim was also supported by BMBF under the joint ROMIC-project SPITFIRE (01LG1205A). CAFE-Africa was funded by the Max Planck Society. ND-MAX was funded by the NASA Advanced Air Vehicles Program (program manager J. Dryer). Funding for NETCARE was provided by the Natural Sciences and Engineering Research Council of Canada through the NETCARE project of the Climate Change and Atmospheric Research Program. The measurements at Jungfraujoch were funded by the DFG grant SCHN1138/2-2 (FOR1525 "INUIT") and by the EU Horizon 2020 research and innovation programme, grant No. 654109 (ACTRIS-2). We also acknowledge that the International Foundation High Altitude Research Stations Jungfraujoch and Gornergrat (HFSJG), 3012 Bern, Switzerland, made it possible for us to carry out our experiment at the

High Altitude Research Station at Jungfraujoch. The Swiss Federal Laboratories for Materials Science and Technology (EMPA) is acknowledged for providing ozone data for the Jungfraujoch through the EBAS/EMEP data base. We acknowledge the NOAA Air Resources Laboratory (ARL) for the provision of the HYSPLIT transport and dispersion model and/or READY website (http://www.ready.noaa.gov) used in this publication. We thank the technical and scientific coordinators of the aircraft campaigns: C. Voigt, A. Minikin, U. Schumann (ML-CIRRUS), J. Lelieveld, H. Fischer, J. Williams, M. Dorf (CAFE-Africa), B. Anderson, T. Moes (ND-MAX/ECLIF-2), F. Stroh, M. Rex, F. Cairo (StratoClim), A. Herber, J. Abbatt, R. Leaitch (NETCARE). We also thank all aircraft crews, campaign teams and hangar staff (especially the staff of 120 ATW (Air Training Wing) at Kalamata), as well as the technical staff at MPIC for support during instrument development and operation during field campaigns. The data shown in this study are available at Edmond – the Open Access Data Repository of the Max Planck Society, under the following permanent link: https://edmond.mpdl.mpg.de/imeji/collection/0VKpFxkQyIcMCSKJ

References

Abbatt, J. P. D., et al. (2019), Overview paper: New insights into aerosol and climate in the Arctic, *Atmos. Chem. Phys.*, *19*(4), 2527-2560, doi:10.5194/acp-19-2527-2019.

Afchine, A., et al. (2018), Ice particle sampling from aircraft – influence of the probing position on the ice water content, *Atmos. Meas. Tech.*, *11*(7), 4015-4031, doi:10.5194/amt-11-4015-2018.

Alpers, M., M. Gerding, J. Höffner, and J. Schneider (2001), Multiwavelength lidar observation of a strange noctilucent cloud at Kühlungsborn, Germany (54°N), *Journal of Geophysical Research: Atmospheres*, *106*(D8), 7945-7953, doi:doi:10.1029/2000JD900666.

Andersson, S. M., B. G. Martinsson, J. Friberg, C. A. M. Brenninkmeijer, A. Rauthe-Schoch, M. Hermann, P. F. J. van Velthoven, and A. Zahn (2013), Composition and evolution of volcanic aerosol from eruptions of Kasatochi, Sarychev and Eyjafjallajokull in 2008-2010 based on CARIBIC observations, *Atmospheric Chemistry and Physics*, *13*(4), 1781-1796, doi:10.5194/acp-13-1781-2013.

Andreae, M. O., et al. (2018), Aerosol characteristics and particle production in the upper troposphere over the Amazon Basin, *Atmos. Chem. Phys.*, *18*(2), 921-961, doi:10.5194/acp-18-921-2018.

Arnold, F., J. Curtius, S. Spreng, and T. Deshler (1998), Stratospheric aerosol sulfuric acid: First direct in situ measurements using a novel balloon-based mass spectrometer apparatus, *J. Atmos. Chem.*, *30*(1), 3-10, doi:10.1023/a:1006067511568.

Bezdek, J. C., R. Ehrlich, and W. Full (1984), FCM: The fuzzy c-means clustering algorithm, *Computers & Geosciences*, *10*(2), 191-203, doi:10.1016/0098-3004(84)90020-7.

Brands, M., et al. (2011), Characterization of a Newly Developed Aircraft-Based Laser Ablation Aerosol Mass Spectrometer (ALABAMA) and First Field Deployment in Urban Pollution Plumes over Paris During MEGAPOLI 2009, *Aerosol Sci. Technol.*, *45*, 46-64, doi:10.1080/02786826.2010.517813.

Bukowiecki, N., E. Weingartner, M. Gysel, M. C. Coen, P. Zieger, E. Herrmann, M. Steinbacher, H. W. Gäggeler, and U. Baltensperger (2016), A Review of More than 20 Years of Aerosol Observation at the High Altitude Research Station Jungfraujoch, Switzerland (3580 m asl), *Aerosol and Air Quality Research*, *16*(3), 764-788, doi:10.4209/aaqr.2015.05.0305.

Burkholder, J. B., M. Mills, and S. McKeen (2000), Upper limit for the UV absorption cross sections of H2SO4, *Geophys. Res. Lett.*, *27*(16), 2493-2496, doi:10.1029/1999GL011271.

Carrillo-Sánchez, J. D., D. Nesvorný, P. Pokorný, D. Janches, and J. M. C. Plane (2016), Sources of cosmic dust in the Earth's atmosphere, *Geophys. Res. Lett.*, *43*(23), 11,979-911,986, doi:doi:10.1002/2016GL071697.

Curtius, J., et al. (2005), Observations of meteoric material and implications for aerosol nucleation in the winter Arctic lower stratosphere derived from in situ particle measurements, *Atmospheric Chemistry and Physics*, *5*, 3053-3069.

Cziczo, D. J., D. M. Murphy, P. K. Hudson, and D. S. Thomson (2004), Single particle measurements of the chemical composition of cirrus ice residue during CRYSTAL-FACE, *J. Geophys. Res.-Atmos.*, *109*(D4), doi:D04201 10.1029/2003jd004032.

Cziczo, D. J., D. M. Murphy, D. S. Thomson, and M. N. Ross (2002), Composition of individual particles in the wakes of an Athena II rocket and the space shuttle, *Geophys. Res. Lett.*, *29*(21), 33-31-33-34, doi:10.1029/2002GL015991.

Cziczo, D. J., D. S. Thomson, and D. M. Murphy (2001), Ablation, flux, and atmospheric implications of meteors inferred from stratospheric aerosol, *Science*, *291*(5509), 1772-1775.

DeCarlo, P. F., J. G. Slowik, D. R. Worsnop, P. Davidovits, and J. L. Jimenez (2004), Particle morphology and density characterization by combined mobility and aerodynamic diameter measurements. Part 1: Theory, *Aerosol Sci. Technol.*, *38*(12), 1185-1205.

Dee, D. P., et al. (2011), The ERA-Interim reanalysis: configuration and performance of the data assimilation system, *Quarterly Journal of the Royal Meteorological Society*, *137*(656), 553-597, doi:10.1002/qj.828.

Diskin, G. S., J. R. Podolske, G. W. Sachse, and T. A. Slate (2002), Open-path airborne tunable diode laser hygrometer, in *Diode Lasers and Applications in Atmospheric Sensing*, edited by A. Fried, Proceedings of the Society of Photo-Optical Instrumentation Engineers (SPIE).

Ebert, M., R. Weigel, K. Kandler, G. Günther, S. Molleker, J. U. Grooß, B. Vogel, S. Weinbruch, and S. Borrmann (2016), Chemical analysis of refractory stratospheric aerosol particles collected within the arctic vortex and inside polar stratospheric clouds, *Atmos. Chem. Phys.*, *16*(13), 8405-8421, doi:10.5194/acp-16-8405-2016.

Eriksen Hammer, S., S. Mertes, J. Schneider, M. Ebert, K. Kandler, and S. Weinbruch (2018), Composition of ice particle residuals in mixed phase clouds at Jungfraujoch (Switzerland): Enrichment and depletion of particle groups relative to total aerosol, *Atmos. Chem. Phys.*, *2018*, 13987–14003, doi:10.5194/acp-18-13987-2018.

Fischer, H., F. G. Wienhold, P. Hoor, O. Bujok, C. Schiller, P. Siegmund, M. Ambaum, H. A. Scheeren, and J. Lelieveld (2000), Tracer correlations in the northern high latitude lowermost stratosphere: Influence of cross-tropopause mass exchange, *Geophys. Res. Lett.*, *27*(1), 97-100, doi:10.1029/1999gl010879.

Froyd, K. D., et al. (2019), A new method to quantify mineral dust and other aerosol species from aircraft platforms using single-particle mass spectrometry, *Atmos. Meas. Tech.*, *2019*, 6209-6239, doi:10.5194/amt-12-6209-2019.

Froyd, K. D., D. M. Murphy, T. J. Sanford, D. S. Thomson, J. C. Wilson, L. Pfister, and L. Lait (2009), Aerosol composition of the tropical upper troposphere, *Atmospheric Chemistry and Physics*, *9*(13), 4363-4385.

Fueglistaler, S., A. E. Dessler, T. J. Dunkerton, I. Folkins, Q. Fu, and P. W. Mote (2009), TROPICAL TROPOPAUSE LAYER, *Reviews of Geophysics*, *47*, doi:10.1029/2008rg000267.

Gabrielli, P., et al. (2004), Meteoric smoke fallout over the Holocene epoch revealed by iridium and platinum in Greenland ice, *Nature*, *432*(7020), 1011-1014, doi:10.1038/nature03137.

Gabrielli, P., et al. (2006), A climatic control on the accretion of meteoric and super-chondritic iridium-platinum to the Antarctic ice cap, *Earth and Planetary Science Letters*, *250*(3-4), 459-469, doi:10.1016/j.epsl.2006.08.015.

Gallavardin, S., U. Lohmann, and D. Cziczo (2008), Analysis and differentiation of mineral dust by single particle laser mass spectrometry, *Int. J. Mass Spectrom.*, *274*(1), 56-63, doi:10.1016/j.ijms.2008.04.031.

Gandrud, B. W., P. D. Sperry, L. Sanford, K. K. Kelly, G. V. Ferry, and K. R. Chan (1989), Filter measurement results from the airborne Antarctic ozone experiment, *J. Geophys. Res.-Atmos.*, *94*(D9), 11285-11297, doi:10.1029/JD094iD09p11285.

Garny, H., T. Birner, H. Bönisch, and F. Bunzel (2014), The effects of mixing on age of air, *Journal of Geophysical Research: Atmospheres*, *119*(12), 7015-7034, doi:10.1002/2013JD021417.

Gettelman, A., P. Hoor, L. L. Pan, W. J. Randel, M. I. Hegglin, and T. Birner (2011), The extratropical upper troposphere and lower stratosphere, *Reviews of Geophysics*, *49*(3), doi:10.1029/2011RG000355.

Gettelman, A., X. Liu, D. Barahona, U. Lohmann, and C. Chen (2012), Climate impacts of ice nucleation, *Journal of Geophysical Research: Atmospheres*, *117*, D20201, doi:doi:10.1029/2012JD017950.

Grooß, J. U., et al. (2014), Nitric acid trihydrate nucleation and denitrification in the Arctic stratosphere, *Atmos. Chem. Phys.*, *14*(2), 1055-1073, doi:10.5194/acp-14-1055-2014.

Gumbel, J., and L. Megner (2009), Charged meteoric smoke as ice nuclei in the mesosphere: Part 1—A review of basic concepts, *J. Atmos. Sol.-Terr. Phys.*, *71*(12), 1225-1235, doi:10.1016/j.jastp.2009.04.012.

Gunsch, M. J., N. W. May, M. Wen, C. L. H. Bottenus, D. J. Gardner, T. M. VanReken, S. B. Bertman, P. K. Hopke, A. P. Ault, and K. A. Pratt (2018), Ubiquitous influence of wildfire emissions and secondary organic aerosol on summertime atmospheric aerosol in the forested Great Lakes region, *Atmos. Chem. Phys.*, *18*(5), 3701-3715, doi:10.5194/acp-18-3701-2018.

Gute, E., et al. (2019), Field evaluation of a Portable Fine Particle Concentrator (PFPC) for ice nucleating particle measurements, *Aerosol Sci. Technol.*, 1-12, doi:10.1080/02786826.2019.1626346.

Hegglin, M. I., D. Brunner, T. Peter, P. Hoor, H. Fischer, J. Staehelin, M. Krebsbach, C. Schiller, U. Parchatka, and U. Weers (2006), Measurements of NO, NOy, N2O, and O3 during SPURT: implications for transport and chemistry in the lowermost stratosphere, *Atmos. Chem. Phys.*, *6*(5), 1331-1350, doi:10.5194/acp-6-1331-2006.

Heller, R., et al. (2017), Mountain waves modulate the water vapor distribution in the UTLS, *Atmos. Chem. Phys.*, *17*(24), 14853-14869, doi:10.5194/acp-17-14853-2017.

Hervig, M. E., J. S. A. Brooke, W. Feng, C. G. Bardeen, and J. M. C. Plane (2017), Constraints on Meteoric Smoke Composition and Meteoric Influx Using SOFIE Observations With Models, *Journal of Geophysical Research: Atmospheres*, *122*(24), 13,495-413,505, doi:10.1002/2017JD027657.

Hervig, M. E., L. E. Deaver, C. G. Bardeen, J. M. Russell, S. M. Bailey, and L. L. Gordley (2012), The content and composition of meteoric smoke in mesospheric ice particles from SOFIE observations, *J. Atmos. Sol.-Terr. Phys.*, *84-85*, 1-6, doi:10.1016/j.jastp.2012.04.005.

Hicks, T. R., B. H. May, and N. K. Reay (1972), MgI emission in night-sky spectrum, *Nature*, *240*(5381), 401-&, doi:10.1038/240401a0.

Hinz, K. P., M. Greweling, F. Drews, and B. Spengler (1999), Data processing in on-line laser mass spectrometry of inorganic, organic, or biological airborne particles, *Journal of the American Society for Mass Spectrometry*, *10*(7), 648-660, doi:10.1016/s1044-0305(99)00028-8.

Holton, J. R., P. H. Haynes, M. E. McIntyre, A. R. Douglass, R. B. Rood, and L. Pfister (1995), Stratosphere-troposphere exchange, *Reviews of Geophysics*, *33*(4), 403-439, doi:10.1029/95rg02097.

Hoor, P., H. Fischer, L. Lange, J. Lelieveld, and D. Brunner (2002), Seasonal variations of a mixing layer in the lowermost stratosphere as identified by the CO-O-3 correlation from in situ measurements, *J. Geophys. Res.-Atmos.*, *107*(D5-6), doi:10.1029/2000jd000289.

Hoor, P., C. Gurk, D. Brunner, M. I. Hegglin, H. Wernli, and H. Fischer (2004), Seasonality and extent of extratropical TST derived from in-situ CO measurements during SPURT, *Atmospheric Chemistry and Physics*, *4*, 1427-1442, doi:10.5194/acp-4-1427-2004.

Hoor, P., H. Wernli, M. I. Hegglin, and H. Bönisch (2010), Transport timescales and tracer properties in the extratropical UTLS, *Atmos. Chem. Phys.*, *10*(16), 7929-7944, doi:10.5194/acp-10-7929-2010.

Höpfner, M., et al. (2019), Ammonium nitrate particles formed in upper troposphere from ground ammonia sources during Asian monsoons, *Nature Geoscience*, *12*(8), 608-612, doi:10.1038/s41561-019-0385-8.

Hoppe, P. (2009), 4.3.3 Meteorites, in *Solar System*, edited by J. E. Trümper, pp. 582-602, Springer Berlin Heidelberg, Berlin, Heidelberg, doi:10.1007/978-3-540-88055-4_30.

Hoskins, B. J., M. E. McIntyre, and A. W. Robertson (1985), On the use and significance of isentropic potential vorticity maps, *Quarterly Journal of the Royal Meteorological Society*, *111*(470), 877-946, doi:10.1256/smsqj.47001.

James, A. D., J. S. A. Brooke, T. P. Mangan, T. F. Whale, J. M. C. Plane, and B. J. Murray (2018), Nucleation of nitric acid hydrates in polar stratospheric clouds by meteoric material, *Atmos. Chem. Phys.*, *18*(7), 4519-4531, doi:10.5194/acp-18-4519-2018.

Junge, C. E., C. W. Chagnon, and J. E. Manson (1961), A World-wide Stratospheric Aerosol Layer, *Science*, *133*(3463), 1478.

Junge, C. E., and J. E. Manson (1961), Stratospheric aerosol studies, *Journal of Geophysical Research*, *66*(7), 2163-2182, doi:10.1029/JZ066i007p02163.

Köllner, F., et al. (2017), Particulate trimethylamine in the summertime Canadian high Arctic lower troposphere, *Atmos. Chem. Phys.*, *17*(22), 13747-13766, doi:10.5194/acp-17-13747-2017.

Krause, J., P. Hoor, A. Engel, F. Ploger, J. U. Grooss, H. Bonisch, T. Keber, B. M. Sinnhuber, W. Woiwode, and H. Oelhaf (2018), Mixing and ageing in the polar lower stratosphere in winter 2015-2016, *Atmospheric Chemistry and Physics*, *18*(8), 6057-6073, doi:10.5194/acp-18-6057-2018.

Kremser, S., et al. (2016), Stratospheric aerosol—Observations, processes, and impact on climate, *Reviews of Geophysics*, *54*(2), 278-335, doi:10.1002/2015RG000511.
Kunz, A., P. Konopka, R. Muller, and L. L. Pan (2011), Dynamical tropopause based on isentropic potential vorticity gradients, *J. Geophys. Res.-Atmos.*, *116*, doi:10.1029/2010jd014343.
Lanci, L., B. Delmonte, D. V. Kent, V. Maggi, P. E. Biscaye, and J. R. Petit (2012), Magnetization of polar ice: a measurement of terrestrial dust and extraterrestrial fallout, *Quaternary Science Reviews*, *33*, 20-31, doi:10.1016/j.quascirev.2011.11.023.
Lary, D. J., M. P. Chipperfield, J. A. Pyle, W. A. Norton, and L. P. Riishojgaard (1995), 3-dimensional tracer initialization and general diagnostics using equivalent PV latitude-potential-temperature coordinates, *Quarterly Journal of the Royal Meteorological Society*, *121*(521), 187-210.
Lazrus, A. L., B. Gandrud, and R. D. Cadle (1971), Chemical composition of air filtration samples of stratospheric sulfate layer, *Journal of Geophysical Research*, *76*(33), 8083-&, doi:10.1029/JC076i033p08083.
Lazrus, A. L., and B. W. Gandrud (1974), Stratospheric sulfate aerosol, *Journal of Geophysical Research*, *79*(24), 3424-3431, doi:10.1029/JC079i024p03424.
Lazrus, A. L., and B. W. Gandrud (1977), Stratospheric sulfate at high-altitudes, *Geophys. Res. Lett.*, *4*(11), 521-522, doi:10.1029/GL004i011p00521.
Lodders, K., and B. Fegley Jr. (1998), *The Planetary Scientist's Companion*, Oxford University Press, New York, Oxford.
Mahnke, C. (2018), Untersuchungen zu Wolkenbildung und Aerosolmikrophysik in der tropischen Troposphäre und UT/LS: Messtechnik und flugzeuggetragene in-situ Beobachtungen, *PhD Thesis (in German), Johannes Gutenberg University, Mainz, Germany*.
Marcy, T. P., et al. (2007), Measurements of trace gases in the tropical tropopause layer, *Atmos. Environ.*, *41*(34), 7253-7261, doi:10.1016/j.atmosenv.2007.05.032.
McKenna, D. S., J. U. Grooss, G. Gunther, P. Konopka, R. Muller, G. Carver, and Y. Sasano (2002a), A new Chemical Lagrangian Model of the Stratosphere (CLaMS) - 2. Formulation of chemistry scheme and initialization, *J. Geophys. Res.-Atmos.*, *107*(D15), doi:10.1029/2000jd000113.
McKenna, D. S., P. Konopka, J. U. Grooss, G. Gunther, R. Muller, R. Spang, D. Offermann, and Y. Orsolini (2002b), A new Chemical Lagrangian Model of the Stratosphere (CLaMS) - 1. Formulation of advection and mixing, *J. Geophys. Res.-Atmos.*, *107*(D16), doi:10.1029/2000jd000114.
Megner, L., and J. Gumbel (2009), Charged meteoric particles as ice nuclei in the mesosphere: Part 2: A feasibility study, *J. Atmos. Sol.-Terr. Phys.*, *71*(12), 1236-1244, doi:10.1016/j.jastp.2009.05.002.
Megner, L., M. Rapp, and J. Gumbel (2006), Distribution of meteoric smoke - sensitivity to microphysical properties and atmospheric conditions, *Atmos. Chem. Phys.*, *6*(12), 4415-4426, doi:10.5194/acp-6-4415-2006.
Megner, L., D. E. Siskind, M. Rapp, and J. Gumbel (2008), Global and temporal distribution of meteoric smoke: A two-dimensional simulation study, *Journal of Geophysical Research: Atmospheres*, *113*(D3), doi:10.1029/2007JD009054.
Meyer, J., et al. (2015), Two decades of water vapor measurements with the FISH fluorescence hygrometer: a review, *Atmos. Chem. Phys.*, *15*(14), 8521-8538, doi:10.5194/acp-15-8521-2015.
Mossop, S. C. (1965), Stratospheric particles at 20 km altitude, *Geochimica Et Cosmochimica Acta*, *29*(4), 201-&, doi:10.1016/0016-7037(65)90017-7.
Murphy, D. M. (2007), The design of single particle laser mass spectrometers, *Mass Spectrom. Rev.*, *26*(2), 150-165, doi:10.1002/mas.20113.
Murphy, D. M., D. J. Cziczo, P. K. Hudson, and D. S. Thomson (2007), Carbonaceous material in aerosol particles in the lower stratosphere and tropopause region, *J. Geophys. Res.-Atmos.*, *112*(D4), doi:D04203 10.1029/2006jd007297.
Murphy, D. M., K. D. Froyd, J. P. Schwarz, and J. C. Wilson (2014), Observations of the chemical composition of stratospheric aerosol particles, *Quarterly Journal of the Royal Meteorological Society*, *140*(681), 1269-1278, doi:10.1002/qj.2213.
Murphy, D. M., D. S. Thomson, and T. M. J. Mahoney (1998), In situ measurements of organics, meteoritic material, mercury, and other elements in aerosols at 5 to 19 kilometers, *Science*, *282*(5394), 1664-1669.
Neu, J. L., and R. A. Plumb (1999), Age of air in a “leaky pipe” model of stratospheric transport, *Journal of Geophysical Research: Atmospheres*, *104*(D16), 19243-19255, doi:10.1029/1999JD900251.
Pan, L. L., S. B. Honomichl, D. E. Kinnison, M. Abalos, W. J. Randel, J. W. Bergman, and J. Bian (2016), Transport of chemical tracers from the boundary layer to stratosphere associated with the dynamics of the Asian summer monsoon, *J. Geophys. Res.-Atmos.*, *121*(23), 14159-14174, doi:10.1002/2016jd025616.
Pan, L. L., L. C. Paulik, S. B. Honomichl, L. A. Munchak, J. C. Bian, H. B. Selkirk, and H. Vomel (2014), Identification of the tropical tropopause transition layer using the ozone-water vapor relationship, *J. Geophys. Res.-Atmos.*, *119*(6), 3586-3599, doi:10.1002/2013jd020558.
Pan, L. L., W. J. Randel, B. L. Gary, M. J. Mahoney, and E. J. Hintsa (2004), Definitions and sharpness of the extratropical tropopause: A trace gas perspective, *J. Geophys. Res.-Atmos.*, *109*(D23), doi:10.1029/2004jd004982.
Plane, J. M. C. (2003), Atmospheric Chemistry of Meteoric Metals, *Chem. Rev.*, *103*(12), 4963-4984, doi:10.1021/cr0205309.
Plane, J. M. C. (2012), Cosmic dust in the earth's atmosphere, *Chem. Soc. Rev.*, *41*(19), 6507-6518, doi:10.1039/C2CS35132C.
Plane, J. M. C., W. Feng, and E. C. M. Dawkins (2015), The Mesosphere and Metals: Chemistry and Changes, *Chem. Rev.*, *115*(10), 4497-4541, doi:10.1021/cr500501m.
Plane, J. M. C., G. J. Flynn, A. Määttänen, J. E. Moores, A. R. Poppe, J. D. Carrillo-Sanchez, and C. Listowski (2018), Impacts of Cosmic Dust on Planetary Atmospheres and Surfaces, *Space Sci. Rev.*, *214*(1), 23, doi:10.1007/s11214-017-0458-1.
Ploeger, F., P. Konopka, K. Walker, and M. Riese (2017), Quantifying pollution transport from the Asian monsoon anticyclone into the lower stratosphere, *Atmos. Chem. Phys.*, *17*(11), 7055-7066, doi:10.5194/acp-17-7055-2017.
Plumb, R. A., W. Heres, J. L. Neu, N. M. Mahowald, J. del Corral, G. C. Toon, E. Ray, F. Moore, and A. E. Andrews (2002), Global tracer modeling during SOLVE: High-latitude descent and mixing, *Journal of Geophysical Research: Atmospheres*, *107*(D5), SOL 52-51-SOL 52-14, doi:10.1029/2001JD001023.
Pommrich, R., et al. (2014), Tropical troposphere to stratosphere transport of carbon monoxide and long-lived trace species in the Chemical Lagrangian Model of the Stratosphere (CLaMS), *Geoscientific Model Development*, *7*(6), 2895-2916, doi:10.5194/gmd-7-2895-2014.
Qin, X., P. V. Bhave, and K. A. Prather (2006), Comparison of Two Methods for Obtaining Quantitative Mass Concentrations from Aerosol Time-of-Flight Mass Spectrometry Measurements, *Anal. Chem.*, *78*(17), 6169-6178, doi:10.1021/ac060395q.

Randel, W. J., M. Park, L. Emmons, D. Kinnison, P. Bernath, K. A. Walker, C. Boone, and H. Pumphrey (2010), Asian Monsoon Transport of Pollution to the Stratosphere, *Science*, *328*(5978), 611-613, doi:10.1126/science.1182274.

Rapp, M., and F. J. Lübken (2004), Polar mesosphere summer echoes (PMSE): Review of observations and current understanding, *Atmos. Chem. Phys.*, *4*(11/12), 2601-2633, doi:10.5194/acp-4-2601-2004.

Rapp, M., J. M. C. Plane, B. Strelnikov, G. Stober, S. Ernst, J. Hedin, M. Friedrich, and U. P. Hoppe (2012), In situ observations of meteor smoke particles (MSP) during the Geminids 2010: constraints on MSP size, work function and composition, *Ann. Geophys.*, *30*(12), 1661-1673, doi:10.5194/angeo-30-1661-2012.

Rapp, M., et al. (2010), Rocket-borne in situ measurements of meteor smoke: Charging properties and implications for seasonal variation, *Journal of Geophysical Research: Atmospheres*, *115*(D1), doi:doi:10.1029/2009JD012725.

Rosen, J. M. (1971), The Boiling Point of Stratospheric Aerosols, *Journal of Applied Meteorology*, *10*(5), 1044-1046, doi:10.1175/1520-0450(1971)010<1044:tbposa>2.0.co;2.

Roth, A., J. Schneider, T. Klimach, S. Mertes, D. van Pinxteren, H. Herrmann, and S. Borrmann (2016), Aerosol properties, source identification, and cloud processing in orographic clouds measured by single particle mass spectrometry on a central European mountain site during HCCT-2010, *Atmos. Chem. Phys.*, *16*(2), 505-524, doi:10.5194/acp-16-505-2016.

Saunders, R. W., S. Dhomse, W. S. Tian, M. P. Chipperfield, and J. M. C. Plane (2012), Interactions of meteoric smoke particles with sulphuric acid in the Earth's stratosphere, *Atmos. Chem. Phys.*, *12*(10), 4387-4398, doi:10.5194/acp-12-4387-2012.

Sedlacek, W. A., E. J. Mroz, A. L. Lazrus, and B. W. Gandrud (1983), A decade of stratospheric sulfate measurements compared with observations of volcanic-eruptions, *Journal of Geophysical Research-Oceans*, *88*(NC6), 3741-3776, doi:10.1029/JC088iC06p03741.

Subasinghe, D., M. D. Campbell-Brown, and E. Stokan (2016), Physical characteristics of faint meteors by light curve and high-resolution observations, and the implications for parent bodies, *Monthly Notices of the Royal Astronomical Society*, *457*(2), 1289-1298, doi:10.1093/mnras/stw019.

Thomson, D. S., A. M. Middlebrook, and D. M. Murphy (1997), Thresholds for laser-induced ion formation from aerosols in a vacuum using ultraviolet and vacuum-ultraviolet laser wavelengths, *Aerosol Sci. Technol.*, *26*(6), 544-559.

Tritscher, I., J. U. Grooß, R. Spang, M. C. Pitts, L. R. Poole, R. Müller, and M. Riese (2019), Lagrangian simulation of ice particles and resulting dehydration in the polar winter stratosphere, *Atmos. Chem. Phys.*, *19*(1), 543-563, doi:10.5194/acp-19-543-2019.

Ulanovsky, A. E., V. A. Yushkov, N. M. Sitnikov, and F. Ravengnani (2001), The FOZAN-II Fast-Response Chemiluminescent Airborne Ozone Analyzer, *Instruments and Experimental Techniques*, *44*(2), 249-256, doi:10.1023/A:1017535608026.

Vernier, J. P., et al. (2009), Tropical stratospheric aerosol layer from CALIPSO lidar observations, *Journal of Geophysical Research: Atmospheres*, *114*(D4), doi:10.1029/2009JD011946.

Vogel, B., R. Müller, G. Günther, R. Spang, S. Hanumanthu, D. Li, M. Riese, and G. P. Stiller (2019), Lagrangian simulations of the transport of young air masses to the top of the Asian monsoon anticyclone and into the tropical pipe, *Atmos. Chem. Phys.*, *19*(9), 6007-6034, doi:10.5194/acp-19-6007-2019.

Voigt, C., et al. (2005), Nitric Acid Trihydrate (NAT) formation at low NAT supersaturation in Polar Stratospheric Clouds (PSCs), *Atmos. Chem. Phys.*, *5*(5), 1371-1380, doi:10.5194/acp-5-1371-2005.

Voigt, C., U. Schumann, K. Graf, and K.-D. Gottschaldt (2013), Impact of rocket exhaust plumes on atmospheric composition and climate — an overview, *EUCASS Proceedings Series – Advances in AeroSpace Sciences*, *4*, 657-670.

Voigt, C., et al. (2017), ML-CIRRUS: The Airborne Experiment on Natural Cirrus and Contrail Cirrus with the High-Altitude Long-Range Research Aircraft HALO, *Bulletin of the American Meteorological Society*, *98*(2), 271-288, doi:10.1175/BAMS-D-15-00213.1.

Vondrak, T., J. M. C. Plane, S. Broadley, and D. Janches (2008), A chemical model of meteoric ablation, *Atmos. Chem. Phys.*, *8*(23), 7015-7031, doi:10.5194/acp-8-7015-2008.

Weger, M., et al. (2018), The impact of mineral dust on cloud formation during the Saharan dust event in April 2014 over Europe, *Atmos. Chem. Phys.*, *18*(23), 17545-17572, doi:10.5194/acp-18-17545-2018.

Weigel, R., C. M. Volk, K. Kandler, E. Hösen, G. Günther, B. Vogel, J. U. Grooß, S. Khaykin, G. V. Belyaev, and S. Borrmann (2014), Enhancements of the refractory submicron aerosol fraction in the Arctic polar vortex: feature or exception?, *Atmos. Chem. Phys.*, *14*(7), 12319–12342, doi:10.5194/acpd-14-12319-2014.

Wilcox, L. J., B. J. Hoskins, and K. P. Shine (2012), A global blended tropopause based on ERA data. Part II: Trends and tropical broadening, *Quarterly Journal of the Royal Meteorological Society*, *138*(664), 576-584, doi:10.1002/qj.910.

Yu, P., et al. (2017), Efficient transport of tropospheric aerosol into the stratosphere via the Asian summer monsoon anticyclone, *Proceedings of the National Academy of Sciences*, *114*(27), 6972, doi:10.1073/pnas.1701170114.

Yue, G. K., L. R. Poole, P. H. Wang, and E. W. Chiou (1994), Stratospheric aerosol acidity, density, and refractive-index deduced from SAGE-II and NMC temperature data, *J. Geophys. Res.-Atmos.*, *99*(D2), 3727-3738, doi:10.1029/93jd02989.

Yushkov, V., A. Oulanovsky, N. Lechenuk, I. Roudakov, K. Arshinov, F. Tikhonov, L. Stefanutti, F. Ravegnani, U. Bonafe, and T. Georgiadis (1999), A Chemiluminescent Analyzer for Stratospheric Measurements of the Ozone Concentration (FOZAN), *Journal of Atmospheric & Oceanic Technology*, *16*(10), 1.

Zahn, A., J. Weppner, H. Widmann, K. Schlote-Holubek, B. Burger, T. Kühner, and H. Franke (2012), A fast and precise chemiluminescence ozone detector for eddy flux and airborne application, *Atmos. Meas. Tech.*, *5*(2), 363-375, doi:10.5194/amt-5-363-2012.

Zöger, M., et al. (1999), Fast in situ stratospheric hygrometers: A new family of balloon-borne and airborne Lyman α photofragment fluorescence hygrometers, *Journal of Geophysical Research: Atmospheres*, *104*(D1), 1807-1816, doi:10.1029/1998JD100025.

Journal of Geophysical Research - Atmospheres

Supporting Information for

Aircraft-based observation of meteoric material in lower stratospheric aerosol particles between 15 and 68°N

Johannes Schneider[1], Ralf Weigel[2], Thomas Klimach[1], Antonis Dragoneas[1,2], Oliver Appel[1,2], Andreas Hünig[1,2], Sergej Molleker[1,2], Franziska Köllner[1], Hans-Christian Clemen[1], Oliver Eppers[1,2], Peter Hoppe[1], Peter Hoor[2], Christoph Mahnke[2,1], Martina Krämer[3], Christian Rolf[3], Jens-Uwe Grooß[3], Andreas Zahn[4], Florian Obersteiner[4], Fabrizio Ravegnani[5], Alexey Ulanovsky[6], Hans Schlager[7], Monika Scheibe[7], Glenn S. Diskin[8], Joshua P. DiGangi[8], John B. Nowak[8], Martin Zöger[9], Stephan Borrmann[2,1]

[1]Particle Chemistry Department, Max Planck Institute for Chemistry, Mainz, Germany

[2]Institute for Physics of the Atmosphere, Johannes Gutenberg University, Mainz, Germany

[3]Forschungszentrum Jülich, Institute of Energy and Climate Research (IEK-7), Jülich, Germany

[4]Karlsruhe Institute of Technology (KIT), Institute for Meteorology and Climate Research, Karlsruhe, Germany

[5]Institute of Atmospheric Sciences and Climate, ISAC-CNR, Bologna, Italy

[6]Central Aerological Observatory, Pervomayskaya 3, Dolgoprudny, Russia

[7]Institute of Atmospheric Physics, German Aerospace Center (DLR) Oberpfaffenhofen, Wessling, Germany

[8]NASA Langley Research Center, MS 483, Hampton, VA, USA

[9]Flight Experiments Department, German Aerospace Center (DLR) Oberpfaffenhofen, Wessling, Germany

Contents of this file

Introduction

This document contains supplementary information, with the objective to give more background information on the data interpretation. It includes the clustering parameters of the single particle data evaluation and the uncertainty estimation (S1). Individual clusters of particles are displayed (S2). The data displayed in Figure 4 of the main text are shown for the individual mission in S3. Section S4 shows the O_3-H_2O tracer-tracer plot for StratoClim 2016 which was not used in the main text. Section S5 explains in more detail the correction for "missed" particles by using the hit rate of the mass spectrometer. The calculation of the sedimentation velocity is explained in S6. An example of sampling line loss calculation is presented in S7. Section S8 shows the results of Mie calculations used to convert the calibration data to real stratospheric refractive indices. Finally, some more information on the detection of meteoric material in tropospheric particles at the Jungfraujoch is present in S9.

S1 Clustering Parameters.

Clustering algorithm and parameters

The individual bipolar mass spectra were sorted using the fuzzy c-means algorithm [*Bezdek et al.*, 1984; *Hinz et al.*, 1999], using the software CRISP that was written at MPIC [*Klimach et al.*, 2010; *Klimach*, 2012; *Roth et al.*, 2016]. The parameters are given in Table S1. Cations were used because the meteoric material is best recognized in the cation spectrum (Fe^+, Mg^+). Preprocessing is done by taking each ion signal to the power of 0.5 to reduce the influence of the signal intensity. The mass spectra were normalized to their sum to reduce the influence of the total ion count per spectrum. Linear correlation was chosen as distance metric (defining "similarity" of the spectra): a Pearson correlation coefficient r = 1 means that two spectra are identical. The number of clusters was prescribed with 20. A set of starting cluster centers was chosen from the data set with the condition that these clusters have Pearson correlation coefficient smaller than 0.9. The fuzzifier (originally introduced as “weighting exponent” by *Bezdek* [1981] represents the fuzziness (blurring, defocusing) of the classification. "Fuzzy abort" parameter defines the stopping criterion of the algorithm, i.e. when the differences between subsequent cluster runs change by less than the chosen value, the algorithm ends.

Variation of clustering parameters

To estimate the influence of the clustering parameters and the chosen sorting algorithm on the number of particles containing meteoric material, six additional different clustering runs were conducted for each UTLS mission. The varied parameters are: number of clusters (10, 20, 30), initialization cluster difference (0.9, 0.7), fuzzyfier (1.3, 1.5), preprocessing (power = 0.5, none), and algorithm type (fuzzy c-means, k-means). Table S2 lists the different runs, the varied parameters and the resulting number of particles containing meteorological material. Criteria for selecting a certain cluster as "containing meteoric material" were 1) high cation signals of Fe^+ and Mg^+ (additionally allowing Na^+, K^+, Al^+), 2) anion signal at HSO_4^-, 3) vertical

profile showing increasing fractional abundance with increasing altitude, potential temperature, or potential vorticity.
In general, the standard deviation is below 6% of the mean value, and the chosen final clustering result using the parameters given in Table S1 (printed in bold) is very close to the mean value.

S2 Individual cluster properties.

Figures S1 through S5 show the particle clusters identified as "containing meteoric material" for the five UTLS aircraft missions.

S3 Theta-latitude histograms for individual aircraft missions.

Figure S6 shows the theta-latitude histograms for the five UTLS aircraft mission. All data were merged to produce Figure 4 of the main text.

S4 Tracer-tracer correlation for StratoClim 2016.

The O_3 and H_2O measurements during StratoClim 2016 did not cover the whole flight time of the three measurement flights. Thus, the data were not used in Figure 8 of the main text, but for completeness are shown here in Figure S7.

S5 ALABAMA hit rate in stratosphere and troposphere.

In section 3.5 of the main text we calculate the absolute number concentrations of particle containing meteoric material. For this, we use the hit rate of the mass spectrometer to estimate the number of "missed" particles. Figure S8 shows the relationship between hit rate and O_3 which allows for estimating the contribution of "invisible" pure H_2SO_4 particle in the stratosphere.

S6 Particle sedimentation in the lower stratosphere.

The time scale for particle sedimentation was calculated as follows:
Pressure, temperature and viscosity of air were taken from the US Standard Atmosphere, using 100 m vertical resolution.
Mean free path (λ), Knudsen number (Kn), Cunningham correction (C_C) and terminal settling velocity (V_{TS}) were calculated using the following equations ([*Hinds*, 1999; *Seinfeld and Pandis*, 2006]):

$\lambda = \frac{1}{\sqrt{2}\pi d_m^2 N}$, with d_m = collision diameter of air molecules (3.7×10^{-10} m), N = number density of air molecules

$Kn = \frac{2\lambda}{d}$ with d = particle diameter

$C_C = 1 + Kn\left(\alpha + \beta e^{-\frac{\gamma}{Kn}}\right)$, with $\alpha = 1.155$, $\beta = 0.471$, $\gamma = 0.596$ (Allan and Raabe, 1982)

$V_{TS} = \frac{\varrho\, d^2\, g\, C_C}{18\, \eta}$, with ϱ = particle density, g = acceleration of gravity, η = viscosity of air.

The terminal settling velocity was calculated for pure H_2SO_4 particles (ρ = 1.83 g cm^{-3}) and pure olivine particles (ρ = 3.30 g cm^{-3}), assuming spherical particle shape. Figure S9 shows the terminal settling velocity as a function of altitude.

S7 Sampling line transmission efficiency.

The sampling line transmission efficiency was calculated here as an example for the configuration of ML-CIRRUS (ALABAMA operated on the HALO aircraft). The ¼" stainless steel sampling line that connected the HALO aerosol submicrometer inlet (HASI, *Wendisch et al.* [2016]; *Andreae et al.* [2018]) line had a total length of 2.9 m with several bends, horizontal and vertical sections. The calculations were done with a modified version of the Particle Loss Calculator (PLC) that was originally described in *von der Weiden et al.* [2009]. The modified version allows for including the sampling line pressure. The results are shown in Figure S10.

S8 Mie calculations for stratospheric aerosol for the optical particle spectrometers OPC 1.129 and UHSAS.

The response of the optical particle spectrometers OPC 1.129 and UHSAS for stratospheric aerosol particles was calculated using an in-house written software [*Vetter*, 2004] following the algorithms described in *Bohren and Huffmann* [1983]. The OPC 1.129 uses a laser wavelength of 655 nm. The scattered light is collected under 90° with an angular range of 60° (i.e. 60° – 120°). The UHSAS uses a laser wavelength of 1054 nm and collects the scattered light in an angular range between 22° and 158°. The refractive index for PSL, m = 1.59, was taken from *Heim et al.* [2008]. The refractive index range (m = 1.43 – 1.45) for lower stratospheric aerosol was taken from *Yue et al.* [1994].
The results (Figure S11) show that the lower size cut off of the OPC shifts from 250 nm to about 285 nm. For the UHSAS, the size channel with lower cut-off of 180 nm (calibrated by PSL) corresponds to 200 nm for stratospheric aerosol particles.

S9 Jungfraujoch backtrajectories, ozone mixing ratio, and meteoric particle fraction.

We inspected backtrajectories to obtain more information on the origin of the meteoric particles detected during the INUIT-2017 campaign at the Jungfraujoch station (3600 m altitude). For this, HYSPLIT [*Stein et al.*, 2015] back trajectories were calculated for 120 – 143 hours using the GDAS 0.5 degree data set. We chose 3600 m a.s.l. as a starting point. 27 trajectories were started per hour, using the trajectory ensemble option. All trajectory data points were binned in altitude and latitude bins and the number of trajectory points per grid is plotted in Figure S12 a) and b). Panel c) of Figure S12 shows the time series of the fraction of meteoric particles detected along with the O_3 mixing ratio. The fraction of meteoric particles is found to be highest between the 18th and 21st of February, a period during which the air mass

spent more time at higher altitudes and latitudes before arriving at the Jungfraujoch. A similar but less pronounced feature is found between 15th and 17th of February. These findings support the conclusion that the origin of this particle type is at higher altitudes. The dependence on latitude can be explained by the fact that mixing between stratosphere and troposphere is stronger at mid-latitudes (see Figure 8 in the main part) than in the tropics. Thus, we would expect to see a higher meteoric particle fraction when the air masses have experienced higher latitudes and altitudes, which is confirmed by Figure S12. Furthermore, a stratospheric origin is supported by the ozone trend in Panel c). The time trend of the meteoric particles follows closely the ozone time series, and even small-scale features (e.g. Feb. 09, Feb. 11, Feb. 16, and Feb. 22) are clearly visible in both time series.

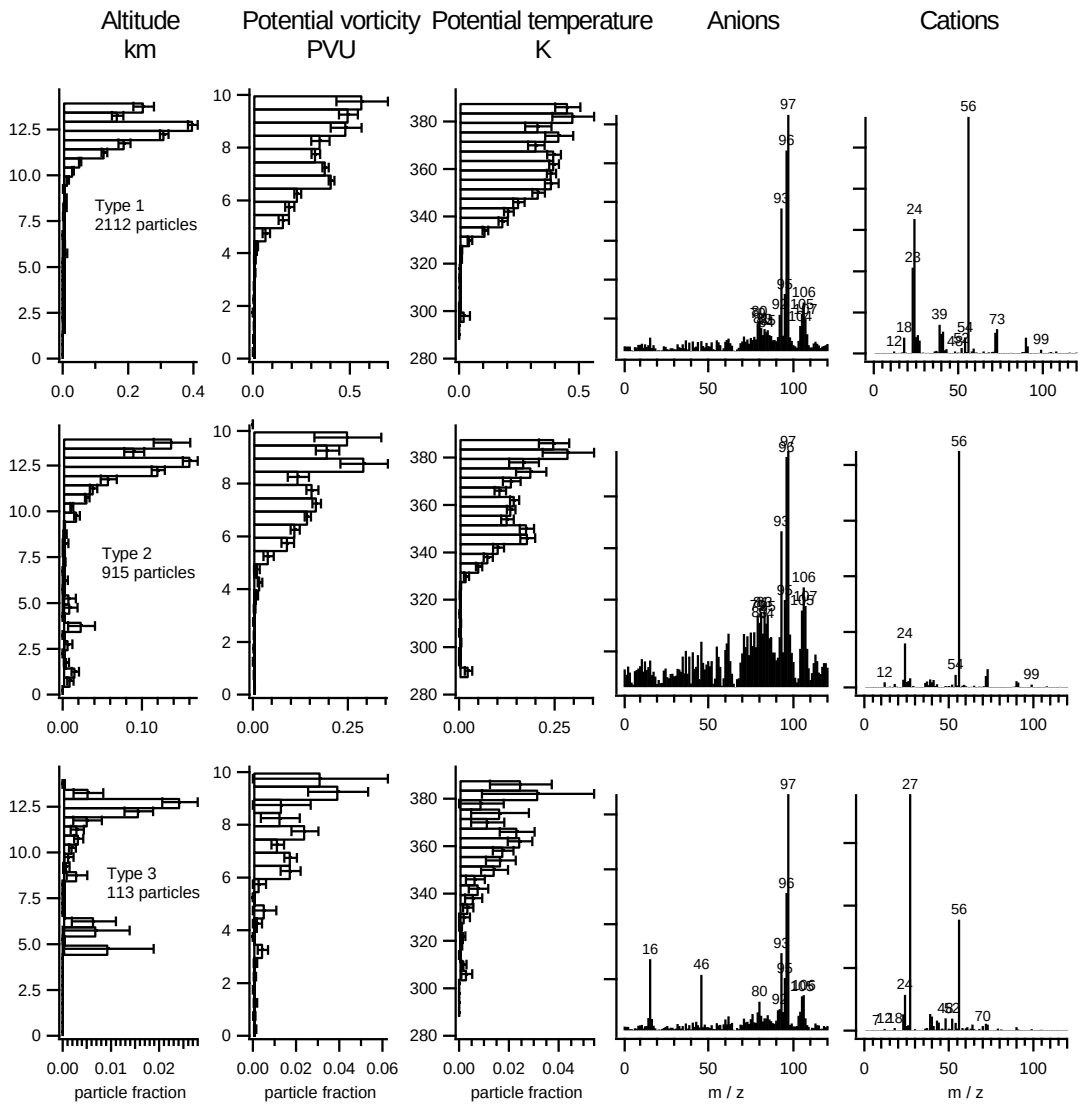

Figure S1. Vertical profiles and mean mass spectra of all clusters from the ML-CIRRUS 2014 data set interpreted as particles containing meteoric material. Note that the negative mass spectra (anions) are noisy, because all anion spectra of each cluster type were averaged for this display, also those where no anion signal was obtained.

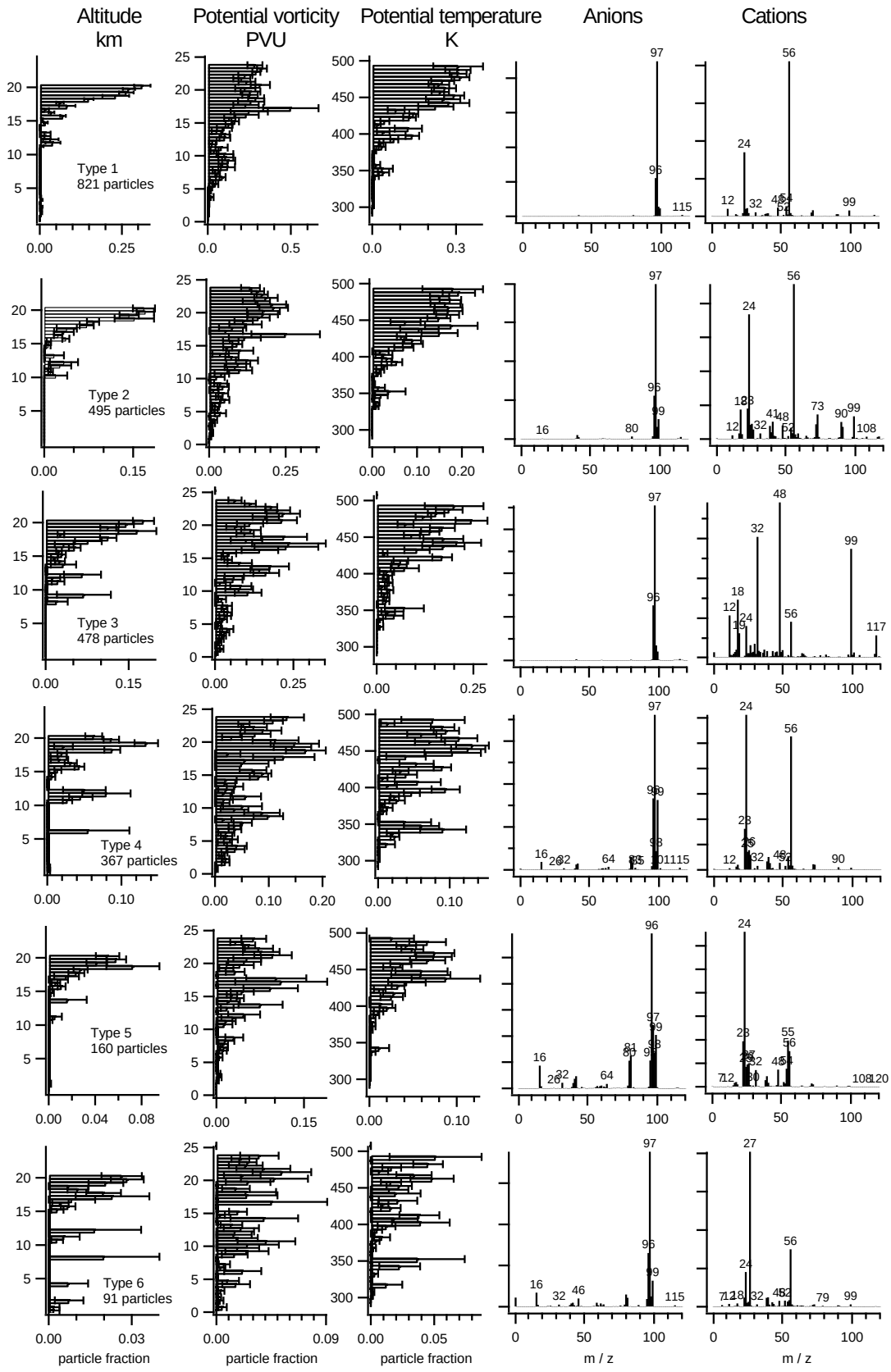
Altitude
km
Potential vorticity
PVU
Potential temperature
K
Anions
Cations
Type 1
821 particles
Type 2
495 particles
Type 3
478 particles
Type 4
367 particles
Type 5
160 particles
Type 6
91 particles
particle fraction
m / z

Figure S2. Vertical profiles and mean mass spectra of all clusters from the StratoClim 2016 data set interpreted as particles containing meteoric material.

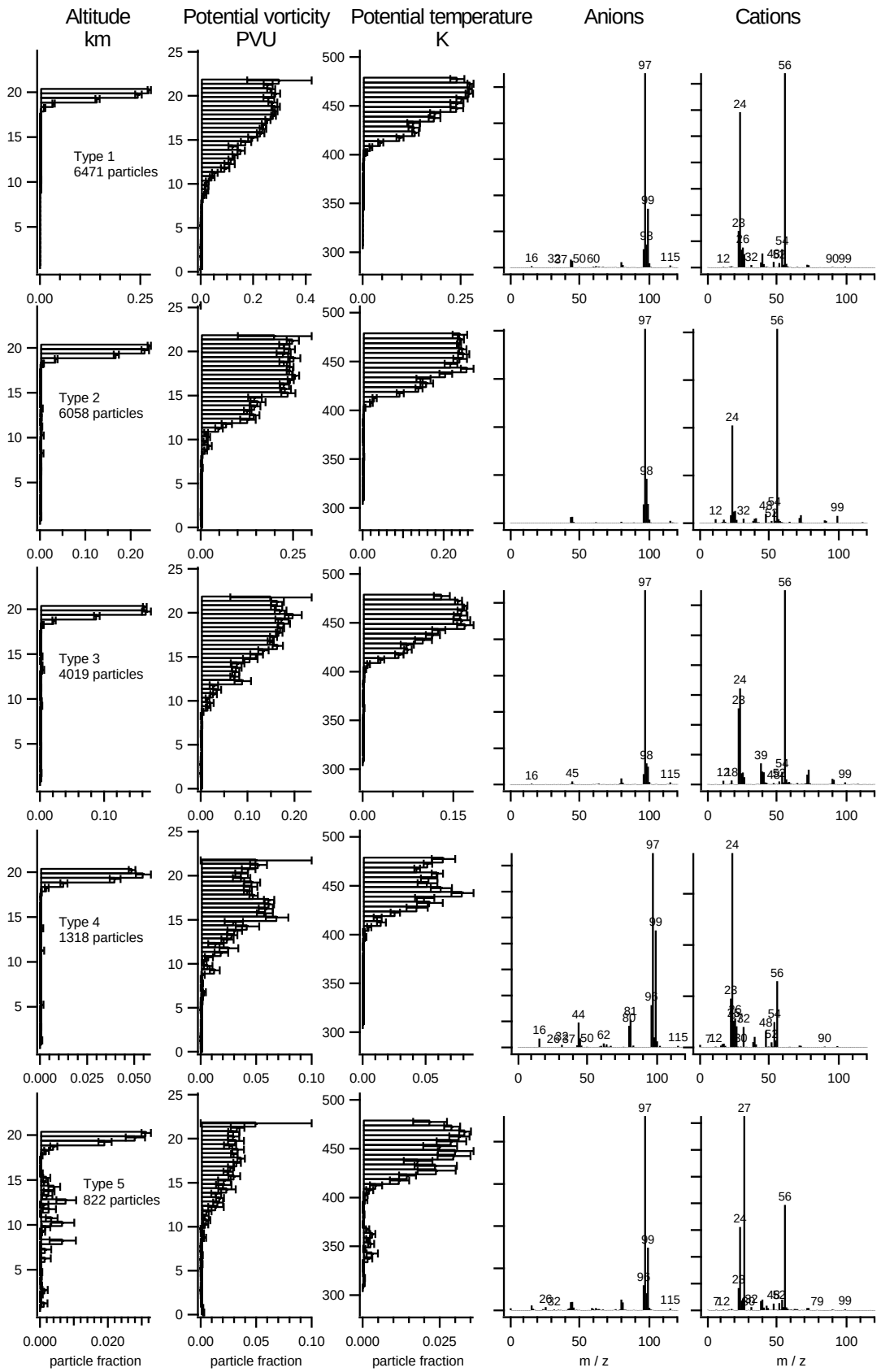
Altitude
km
Potential vorticity
PVU
Potential temperature
K
Anions
Cations
Type 1
6471 particles
Type 2
6058 particles
Type 3
4019 particles
Type 4
1318 particles
Type 5
822 particles
particle fraction
particle fraction
particle fraction
m / z
m / z

Figure S3. Vertical profiles and mean mass spectra of all clusters from the StratoClim 2017 data set interpreted as particles containing meteoric material.

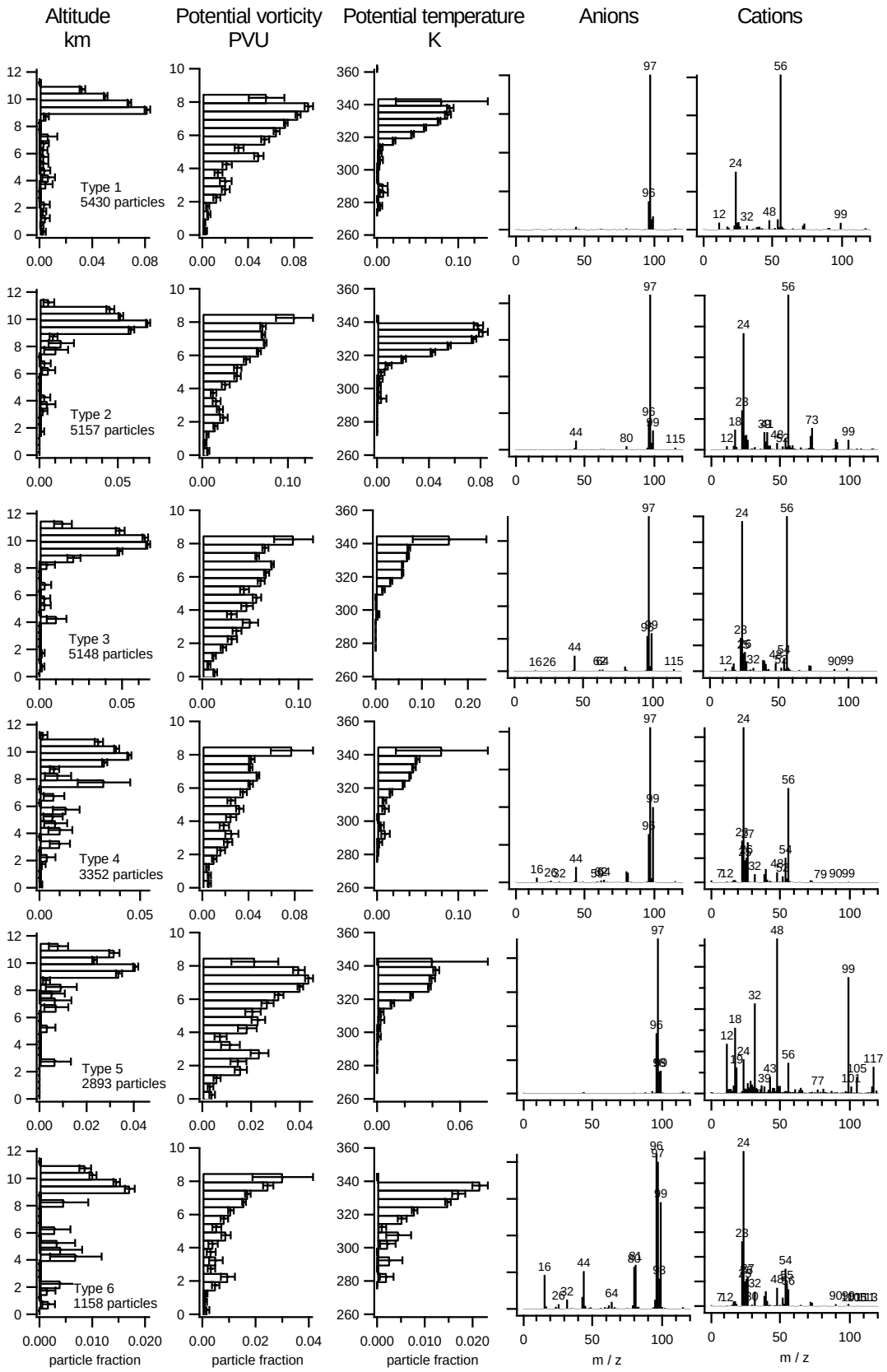
Altitude
km
Potential vorticity
PVU
Potential temperature
K
Anions
Cations
Type 1
5430 particles
Type 2
5157 particles
Type 3
5148 particles
Type 4
3352 particles
Type 5
2893 particles
Type 6
1158 particles
particle fraction
m / z

Figure S4. Vertical profiles and mean mass spectra of all clusters from the ND-MAX/ECLIF-2 data set interpreted as particles containing meteoric material.

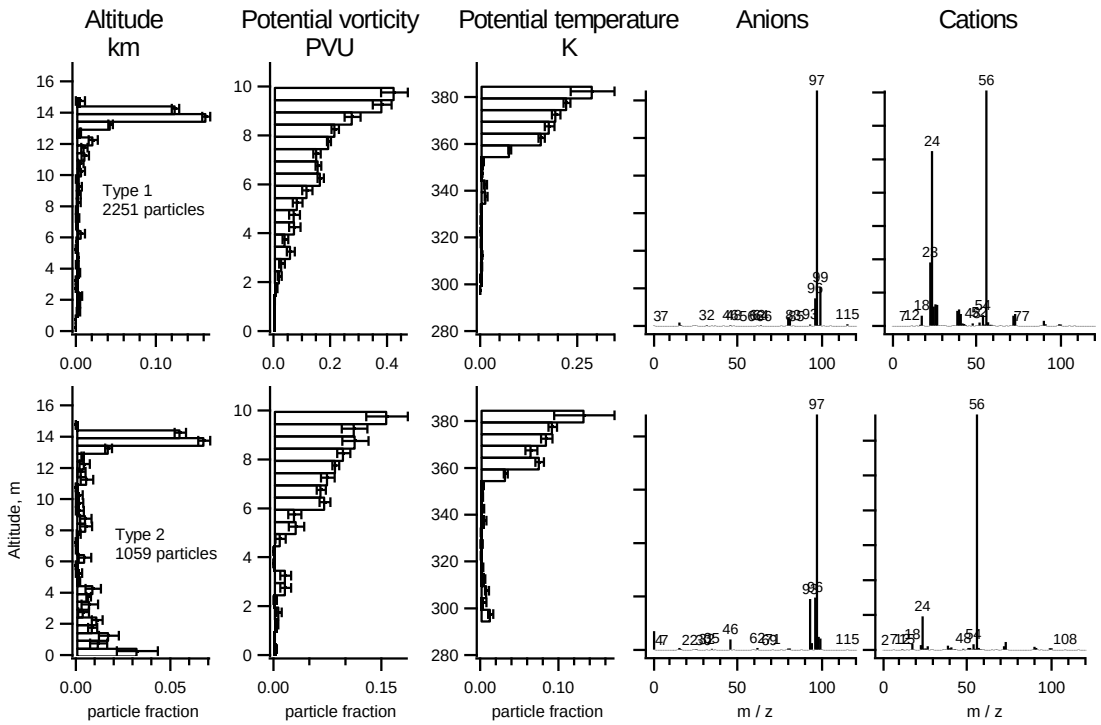

Figure S3. Vertical profiles and mean mass spectra of all clusters from the CAFE-Africa data set interpreted as particles containing meteoric material.

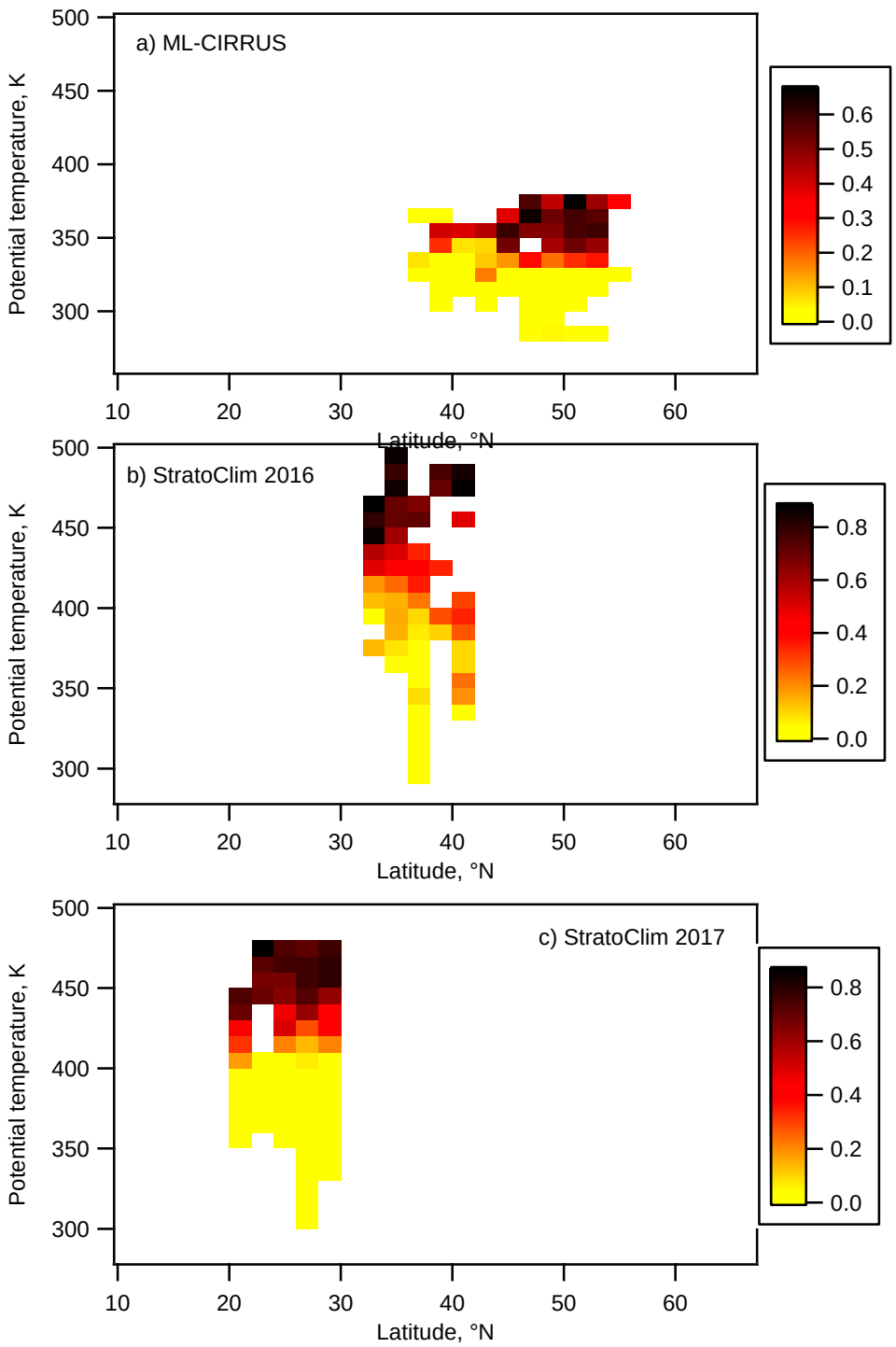
a) ML-CIRRUS
b) StratoClim 2016
c) StratoClim 2017
Potential temperature, K
Latitude, °N
500
450
400
350
300
10
20
30
40
50
60
0.6
0.5
0.4
0.3
0.2
0.1
0.0
0.8
0.6
0.4
0.2
0.0

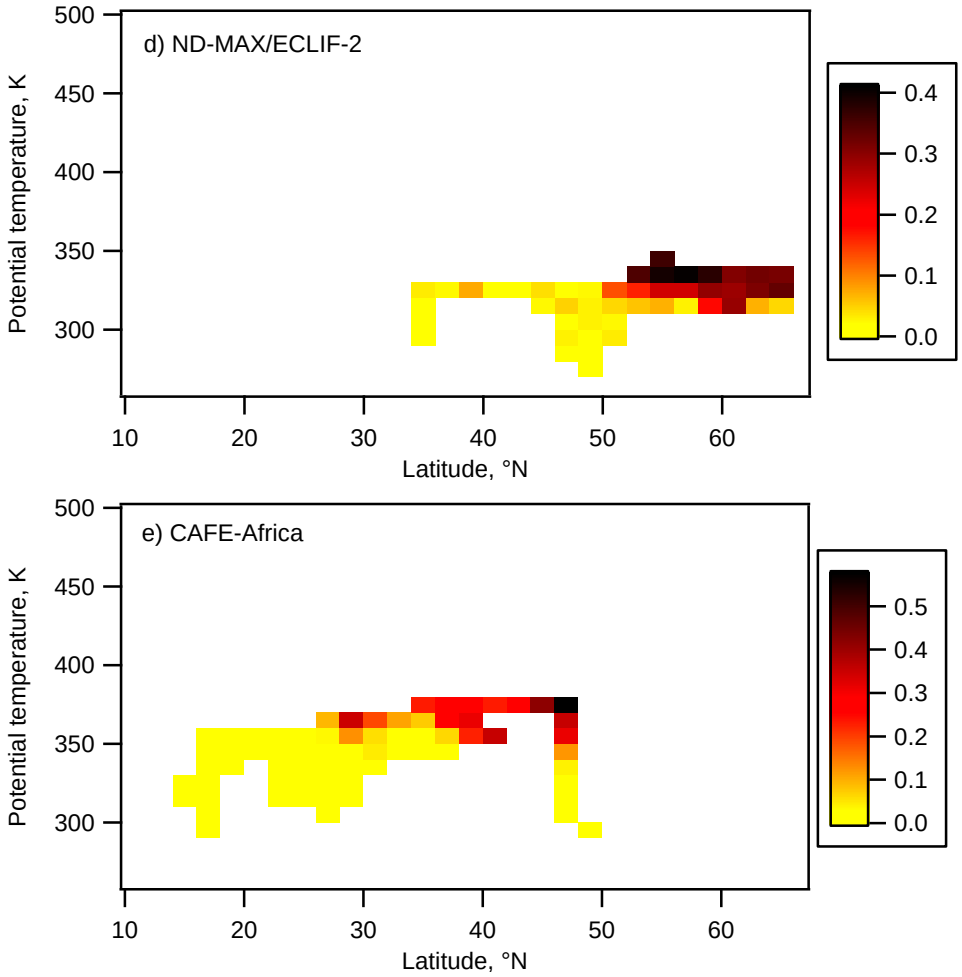

Figure S6. Fraction of meteoric particles as function of potential temperature and latitude for the individual missions: a) ML-CIRRUS, b) StratoClim 2016, c) StratoClim 2017, d) ND-MAX-ECLIF-2, e) CAFE-Africa.

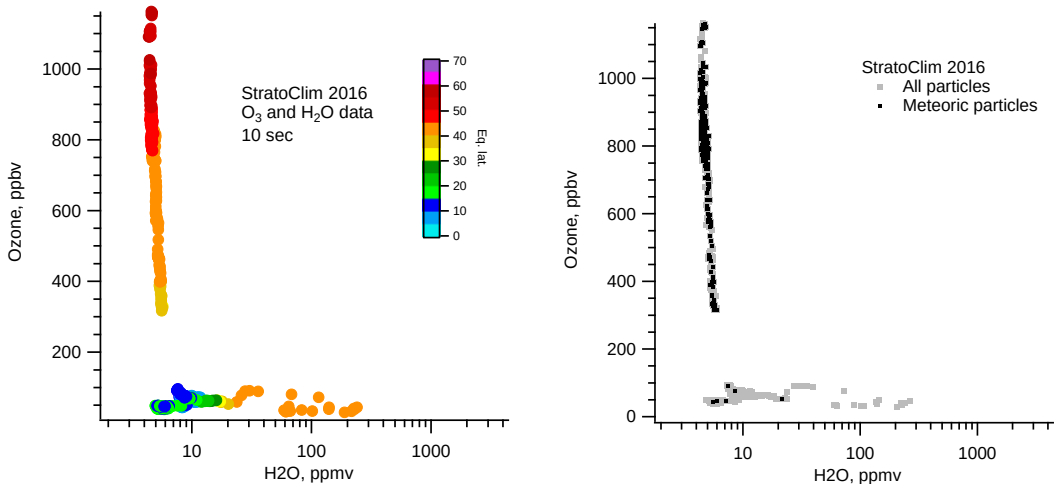

Figure S7. Tracer-tracer correlation for StratoClim 2016. As the instruments were not fully operative during the whole flight time of the three flights of StratoClim 2016, several gaps in the data prevent the analysis of cross-tropopause transport for this mission.

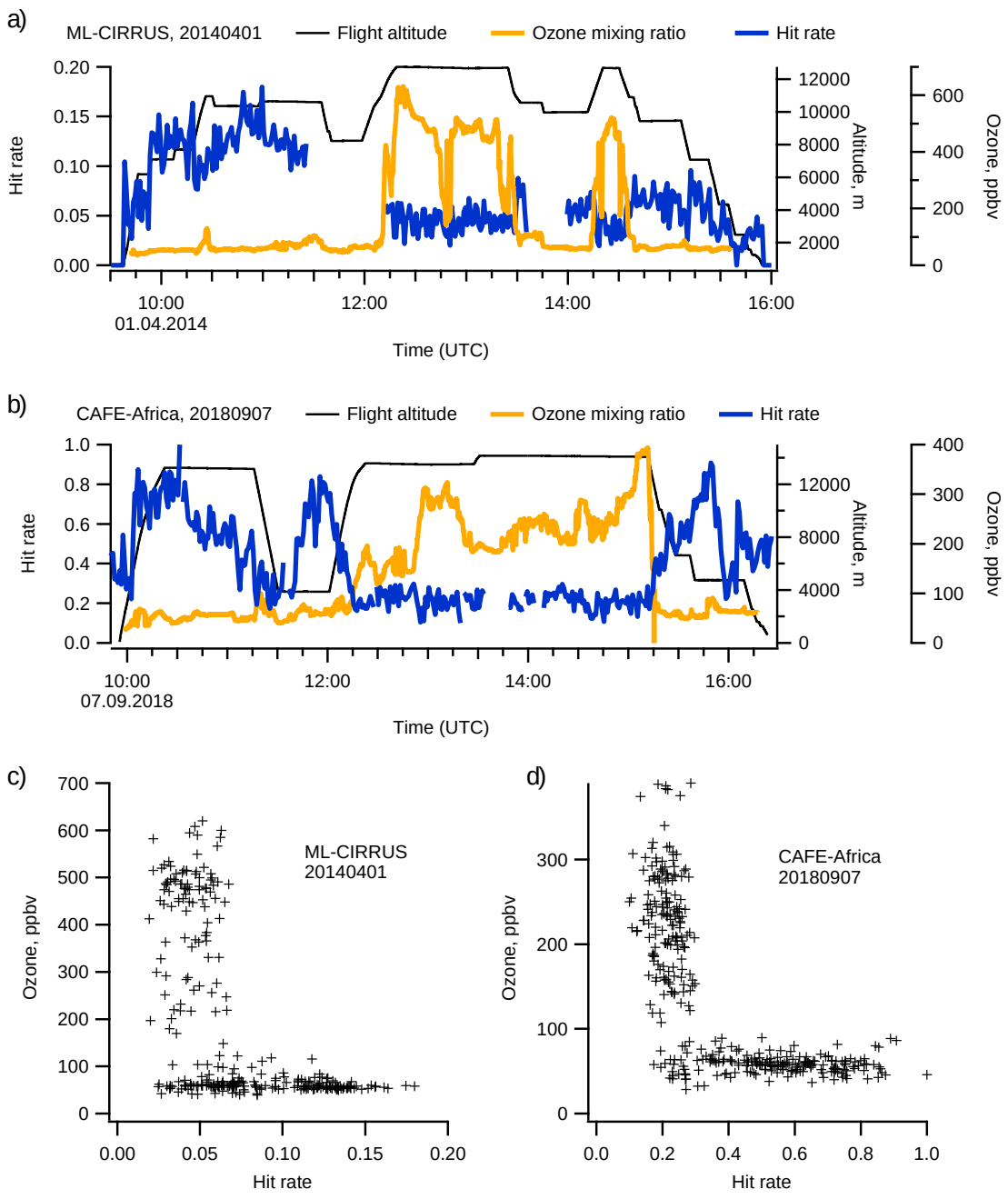

Figure S8. Hit rate (mass spectra per laser shot during time intervals of one minute) of ALABAMA during a) a flight on April 01, 2014 (ML-CIRRUS) and b) a flight on Sept 07, 2018 (CAFE-Africa) as a function of time along with ozone mixing ratio and flight altitude. c) + d): Hit rate versus ozone mixing ratio. Dividing between troposphere and stratosphere at 150 ppbv ozone (ML-CIRRUS) and 100 ppb ozone (CAFE-Africa), respectively, yields an average hit rate in the stratosphere of 0.044 ± 0.012 (ML-CIRRUS) and 0.21 ± 0.04 (CAFE-Africa). For the troposphere, we obtain 0.091 ± 0.037 (ML-CIRRUS) and 0.54 ± 0.18 (CAFE-Africa).

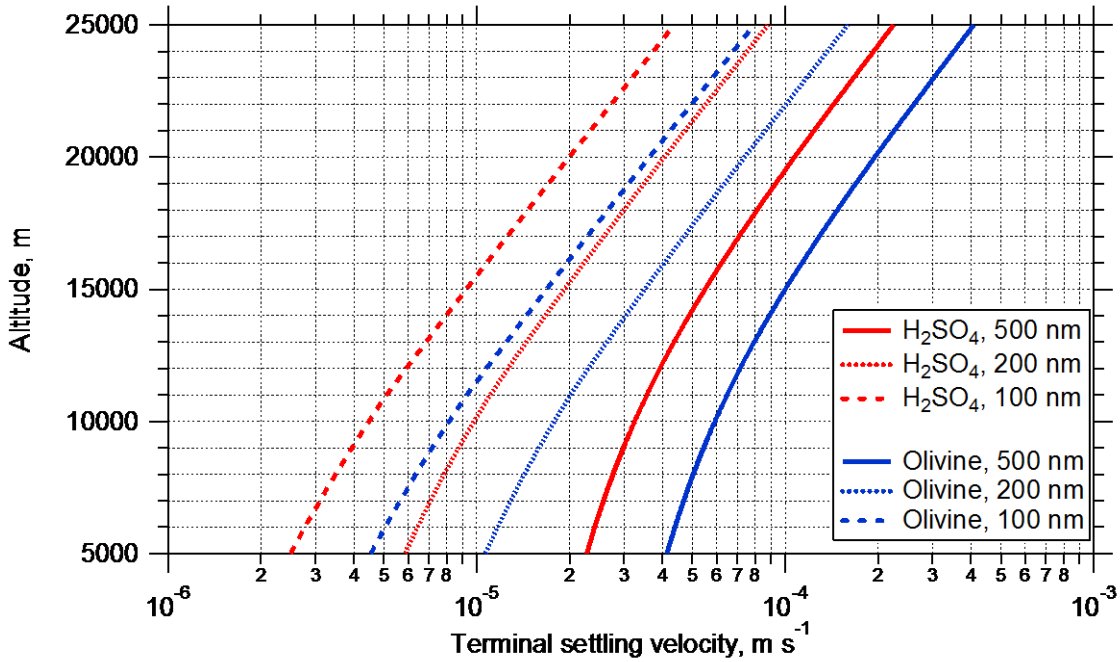

Figure S9. Terminal settling velocity for H2SO4 and olivine particles of 100 , 200, and 500 nm volume equivalent diameter (d_{ve}).

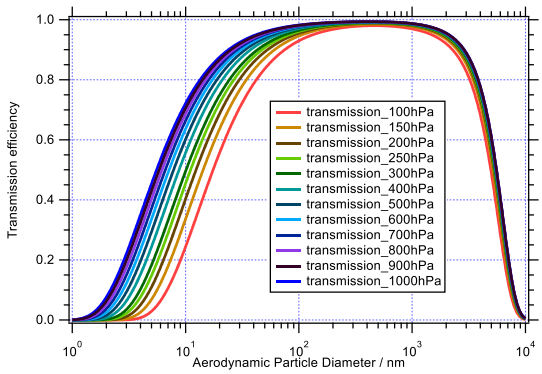

Figure S10. Transmission curves for the sampling line used in ML-CIRRUS that connected the HALO aerosol submicrometer inlet (HASI) to the OPC 1.129 in the ALABAMA rack.

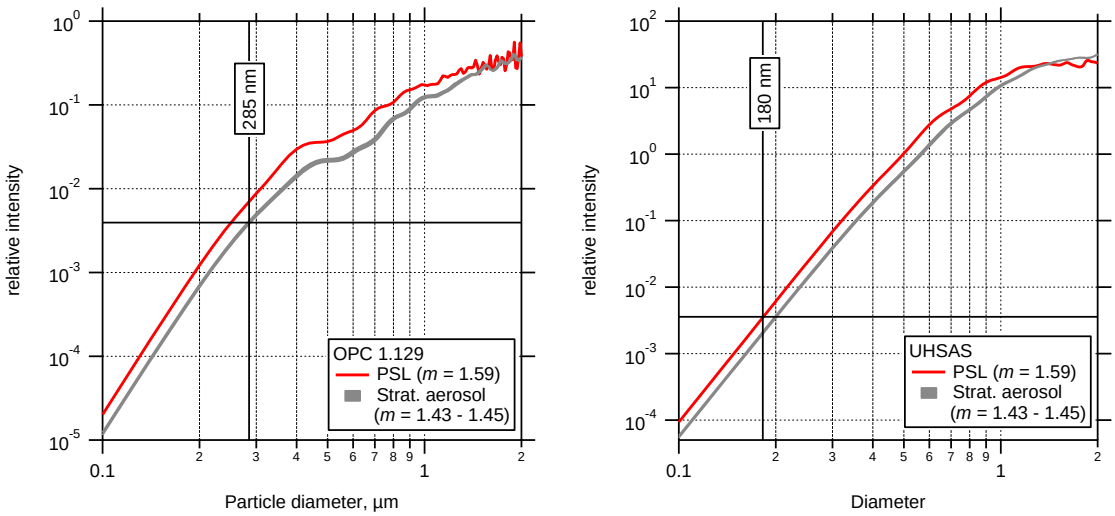

Figure S11. Relative intensity at the detector calculated for the OPC (Grimm 1.129, "Sky-OPC") and for the UHSAS, for PSL particles and for stratospheric particles.

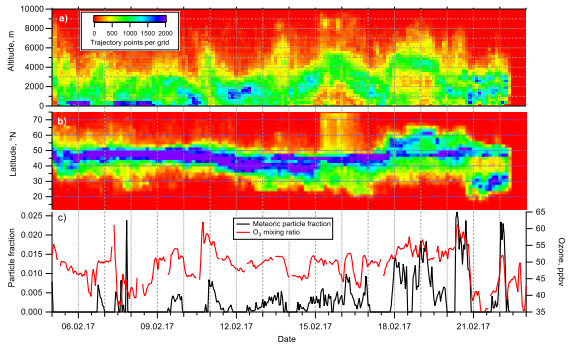

Figure S12. Backtrajectory information for the INUIT-JFJ 2017 field campaign at Jungfraujoch. For each hour, 27 backtrajectories were started using the trajectory ensemble option and were followed for 120 – 143 h using HYSPLIT [Stein et al., 2015] with the GADS 0.5 degree data set. Panel a) shows the number of points during which the trajectories resided in the respective altitude and time grid, Panel b) the same but for latitude. Panel c) shows the number fraction of the meteoric particles along with ozone mixing ratio.

Ion type	Cations
Preprocessing	Power each m/z by 0.5
Normalization	Sum
Distance metric	Correlation
Initialization	Different startclusters:
Number of clusters	20
Cluster difference	0.9
Fuzzifier	1.3
Fuzzy abort	1e-5

Table S1. Clustering parameters used for the final analysis..

Project	Cluster algorithm	Number of clusters	Cluster diff	Fuzzifier	Pre-processing	Number of "meteoric" particles
ML-CIRRUS	Fuzzy c-means	10	0.9	1.3	$(m/z)^{0.5}$	3080
	Fuzzy c-means	**20**	**0.9**	**1.3**	$\mathbf{(m/z)^{0.5}}$	**3140**
	Fuzzy c-means	30	0.9	1.3	$(m/z)^{0.5}$	3136
	Fuzzy c-means	20	0.7	1.3	$(m/z)^{0.5}$	2931
	Fuzzy c-mean	20	0.9	1.5	$(m/z)^{0.5}$	3136
	Fuzzy c-means	20	0.9	1.3	none	3051
	k-means	20	0.9	N/A	$(m/z)^{0.5}$	3247
Mean ± StdDev						3103 ± 90
StratoClim 2016	Fuzzy c-means	10	0.9	1.3	$(m/z)^{0.5}$	2357
	Fuzzy c-means	**20**	**0.9**	**1.3**	$\mathbf{(m/z)^{0.5}}$	**2412**
	Fuzzy c-means	30	0.9	1.3	$(m/z)^{0.5}$	2679
	Fuzzy c-means	20	0.7	1.3	$(m/z)^{0.5}$	2376
	Fuzzy c-mean	20	0.9	1.5	$(m/z)^{0.5}$	2567
	Fuzzy c-means	20	0.9	1.3	none	2618
	k-means	20	0.9	N/A	$(m/z)^{0.5}$	2570
Mean ± StdDev						2511 ± 118
StratoClim 2017	Fuzzy c-means	10	0.9	1.3	$(m/z)^{0.5}$	18355
	Fuzzy c-means	**20**	**0.9**	**1.3**	$\mathbf{(m/z)^{0.5}}$	**18688**
	Fuzzy c-means	30	0.9	1.3	$(m/z)^{0.5}$	19700
	Fuzzy c-means	20	0.7	1.3	$(m/z)^{0.5}$	18688
	Fuzzy c-mean	20	0.9	1.5	$(m/z)^{0.5}$	18459
	Fuzzy c-means	20	0.9	1.3	none	21235
	k-means	20	0.9	N/A	$(m/z)^{0.5}$	20215
Mean ± StdDev						19334 ± 1006
ND-MAX/ ECLIF-2	Fuzzy c-means	10	0.9	1.3	$(m/z)^{0.5}$	20141
	Fuzzy c-means	**20**	**0.9**	**1.3**	$\mathbf{(m/z)^{0.5}}$	**23138**
	Fuzzy c-means	30	0.9	1.3	$(m/z)^{0.5}$	21883
	Fuzzy c-means	20	0.7	1.3	$(m/z)^{0.5}$	21681
	Fuzzy c-mean	20	0.9	1.5	$(m/z)^{0.5}$	21126
	Fuzzy c-means	20	0.9	1.3	none	21752
	k-means	20	0.9	N/A	$(m/z)^{0.5}$	18998
Mean ± StdDev						21245 ± 1237
CAFE-Africa	Fuzzy c-means	10	0.9	1.3	$(m/z)^{0.5}$	3325
	Fuzzy c-means	**20**	**0.9**	**1.3**	$\mathbf{(m/z)^{0.5}}$	**3310**
	Fuzzy c-means	30	0.9	1.3	$(m/z)^{0.5}$	3290
	Fuzzy c-means	20	0.7	1.3	$(m/z)^{0.5}$	3194
	Fuzzy c-mean	20	0.9	1.5	$(m/z)^{0.5}$	3281
	Fuzzy c-means	20	0.9	1.3	none	3287
	k-means	20	0.9	N/A	$(m/z)^{0.5}$	3515
Mean ± StdDev						3314 ± 90

Table S1. Variations of clustering parameters. The inferred number of particles containing meteoric material is given in the last column. Other parameters were kept as in Table S1.

References

Andreae, M. O., et al. (2018), Aerosol characteristics and particle production in the upper troposphere over the Amazon Basin, *Atmos. Chem. Phys.*, *18*(2), 921-961, doi:10.5194/acp-18-921-2018.

Bezdek, J. C. (1981), *Pattern Recognition with Fuzzy Objective Function Algorithms*, Plenum Press, New York, USA.

Bezdek, J. C., R. Ehrlich, and W. Full (1984), FCM: The fuzzy c-means clustering algorithm, *Computers & Geosciences*, *10*(2), 191-203, doi:10.1016/0098-3004(84)90020-7.

Bohren, C. F., and D. R. Huffmann (1983), *Absorption and scattering of light by small particles*, Wiley and Sons, New York.

Heim, M., B. J. Mullins, H. Umhauer, and G. Kasper (2008), Performance evaluation of three optical particle counters with an efficient "multimodal" calibration method, *J. Aerosol. Sci.*, *39*(12), 1019-1031, doi:https://doi.org/10.1016/j.jaerosci.2008.07.006.

Hinds, W. C. (1999), *Aerosol technology - properties, behaviour, and measurements of airborne particles*, 2. ed., John Wiley & Sons, Inc., New York.

Hinz, K. P., M. Greweling, F. Drews, and B. Spengler (1999), Data processing in on-line laser mass spectrometry of inorganic, organic, or biological airborne particles, *Journal of the American Society for Mass Spectrometry*, *10*(7), 648-660, doi:10.1016/s1044-0305(99)00028-8.

Klimach, T. (2012), Chemische Zusammensetzung der Aerosole: Design und Datenauswertung eines Einzelpartikel-Laserablationsmassenspektrometers, Ph.D. thesis (in German), Johannes Gutenberg-Universität, Mainz, Germany, doi:http://nbn-resolving.de/urn:nbn:de:hebis:77-33547.

Klimach, T., F. Drewnick, and S. Borrmann (2010), CRISP - a new tool for analysis of single particle mass spectra, in *International Aerosol Conference*, edited, Helsinki.

Roth, A., J. Schneider, T. Klimach, S. Mertes, D. van Pinxteren, H. Herrmann, and S. Borrmann (2016), Aerosol properties, source identification, and cloud processing in orographic clouds measured by single particle mass spectrometry on a central European mountain site during HCCT-2010, *Atmos. Chem. Phys.*, *16*(2), 505-524, doi:10.5194/acp-16-505-2016.

Seinfeld, J. H., and S. N. Pandis (2006), *Atmospheric chemistry and physics: from air pollution to climate change* John Wiley and Sons, Hoboken, NJ.

Stein, A. F., R. R. Draxler, G. D. Rolph, B. J. B. Stunder, M. D. Cohen, and F. Ngan (2015), NOAA's HYSPLIT Atmospheric Transport and Dispersion Modeling System, *Bulletin of the American Meteorological Society*, *96*(12), 2059-2077, doi:doi:10.1175/BAMS-D-14-00110.1.

Vetter, T. (2004), Berechnung der Mie-Streufunktionen zur Kalibrierung optischer Partikelzähler, *Diploma thesis (in German)*, *University Mainz*.

von der Weiden, S. L., F. Drewnick, and S. Borrmann (2009), Particle Loss Calculator – a new software tool for the assessment of the performance of aerosol inlet systems, *Atmos. Meas. Tech.*, *2*(2), 479-494, doi:10.5194/amt-2-479-2009.

Wendisch, M., et al. (2016), ACRIDICON–CHUVA Campaign: Studying Tropical Deep Convective Clouds and Precipitation over Amazonia Using the New German Research Aircraft HALO, *Bulletin of the American Meteorological Society*, *97*(10), 1885-1908, doi:10.1175/BAMS-D-14-00255.1.

Yue, G. K., L. R. Poole, P. H. Wang, and E. W. Chiou (1994), Stratospheric aerosol acidity, density, and refractive-index deduced from SAGE-II and NMC temperature data, *J. Geophys. Res.-Atmos.*, *99*(D2), 3727-3738, doi:10.1029/93jd02989.